Eddy Vertical Structure and Energy in the Southeastern Indian Ocean: Implications for Dissipation and Lifespan

Yinghui He[1, 2, 3, 4], Wenshuo Ding[1, 5], Qingyou He[1], Xiaoming Zhai[4], Tongya Liu[2, *], Yankun Gong[1], Jieshuo Xie[1], Jiexin Xu[1], Zhiwu Chen[1], Juan Li[1], Pengfei Lin[3], and Shuqun Cai[1, *]

[1]State Key Laboratory of Tropical Oceanography, South China Sea Institute of Oceanology, CAS, 164 West Xingang Road, Guangzhou 510301, China

[2]State Key Laboratory of Satellite Ocean Environment Dynamics, Second Institute of Oceanography, Ministry of Natural Resources, Hangzhou 310000, China

[3] State Key Laboratory of Numerical Modeling for Atmospheric Sciences and Geophysical Fluid Dynamics, Institute of Atmospheric Physics, Chinese Academy of Sciences, Beijing 100029, China

[4] School of Environmental Sciences, Centre for Ocean and Atmospheric Sciences, University of East Anglia, Norwich, United Kingdom

[5] University of Chinese Academy of Sciences, Beijing 100049, China

Corresponding author:

Tongya Liu (liutongya@sio.org.cn); Shuqun Cai (caisq@scsio.ac.cn)

Keywords:

Mesoscale eddies; Eddy vertical structure; Subsurface-intensified eddies; Indian Ocean; Eddy lifespan; Eddy energetics;

Highlights:

- Cyclonic eddies show more regional variations in vertical structure than anticyclonic eddies.
- Eddy vertical structure, associated with occurrence region, plays a pivotal role in regulating eddy energy and lifespan.
- Subsurface-intensified eddies have longer lifespans due to their greater energy and weaker vertical mixing.

Abstract

Satellite observations reveal that mesoscale eddies in the southeastern Indian Ocean (SEIO) are highly active and exhibit pronounced spatial variability in their surface characteristics. By combining satellite and Argo float observations, this study investigates the spatial variations in eddy vertical structure and volume-integrated energy in the SEIO, with particular emphasis on their relationship to eddy lifespan. Cyclonic eddies (CEs) display strong regional contrasts, whereas anticyclonic eddies (AEs) vary less. Subsurface-intensified eddies, predominantly cyclonic, feature a density core near 750 m and maximum velocity at ~250 m depth, and mainly originate from the Leeuwin Current System (LCS) and the open ocean south of 30°S. Eddy lifespan is strongly correlated with volume-integrated energy, which is mainly controlled by eddy amplitude and eddy vertical structure . To further interpret this relationship, we examined energy dissipation terms in the eddy energy equations. The eddy energy dissipation term is expressed as a function of eddy structure, allowing us to quantify regional differences in energy decay rates among eddies with distinct vertical structures. In subsurface-intensified eddies, dissipation due to vertical mixing is much weaker than in surface-intensified eddies. Vertical mixing dissipates eddy potential energy more rapidly than eddy kinetic energy, while horizontal mixing shows the opposite tendency. Overall, CEs in the LCS tend to sustain longer lifespans owing to their higher volume-integrated energy and weaker vertical mixing. These findings underscore the pivotal roles of eddy structure and energy in regulating eddy lifespan.

1 Introduction

Mesoscale eddies (with spatial scales of tens to hundreds of kilometers and lifespans of tens to hundreds of days) contain most of the ocean's kinetic energy (Wunch and Ferrari, 2009). They not only play vital roles in transporting water mass, heat and salt (e.g., Zhang et al., 2014, Dong et al., 2014, and references therein), but also affect the distribution of nutrients and growth of the primary productivity (Patel et al., 2020). Satellite observations show that the eddy kinetic energy (EKE) is considerable in the subtropical Southeastern Indian Ocean (SEIO) (Fig. 1a), where eddy-induced horizontal and vertical transports play pivotal roles in the water mass distribution, primary productivity and climate change (Dufois et al., 2014; Qu et al., 2019; Guo et al., 2020; Liu and Abernathey, 2023). Mesoscale eddies in the SEIO predominantly originate from two key current systems: South Indian Countercurrent system (SICCS) in the open ocean and Leeuwin Current system (LCS) in the eastern boundary of the SEIO (Zhang et al., 2020). The SICCS consists of the shallow eastward South Indian Countercurrent, which is largely confined to the upper 200–250 m, and the underlying westward South Equatorial Current. The main branch of the SEC is located between 10°S and 20°S and extends southward beneath the SICC, with westward flow occurring from approximately 350 m to at least 1100 m depth (Palastanga et al., 2007; Talley et al., 2011; Phillips et al., 2021). The LCS is composed of the surface (shallower than 300 m) poleward Leeuwin Current and the subsurface (about 300 to 800 m) equatorward Leeuwin Undercurrent. Both the SICCS and LCS experience the growth of strong baroclinic and/or barotropic instabilities (Batteen and Butler, 1998; Feng et al., 2005; Rennie et al., 2007; Jia et al., 2011), resulting in elevated mesoscale eddy processes that shape the SEIO environment.

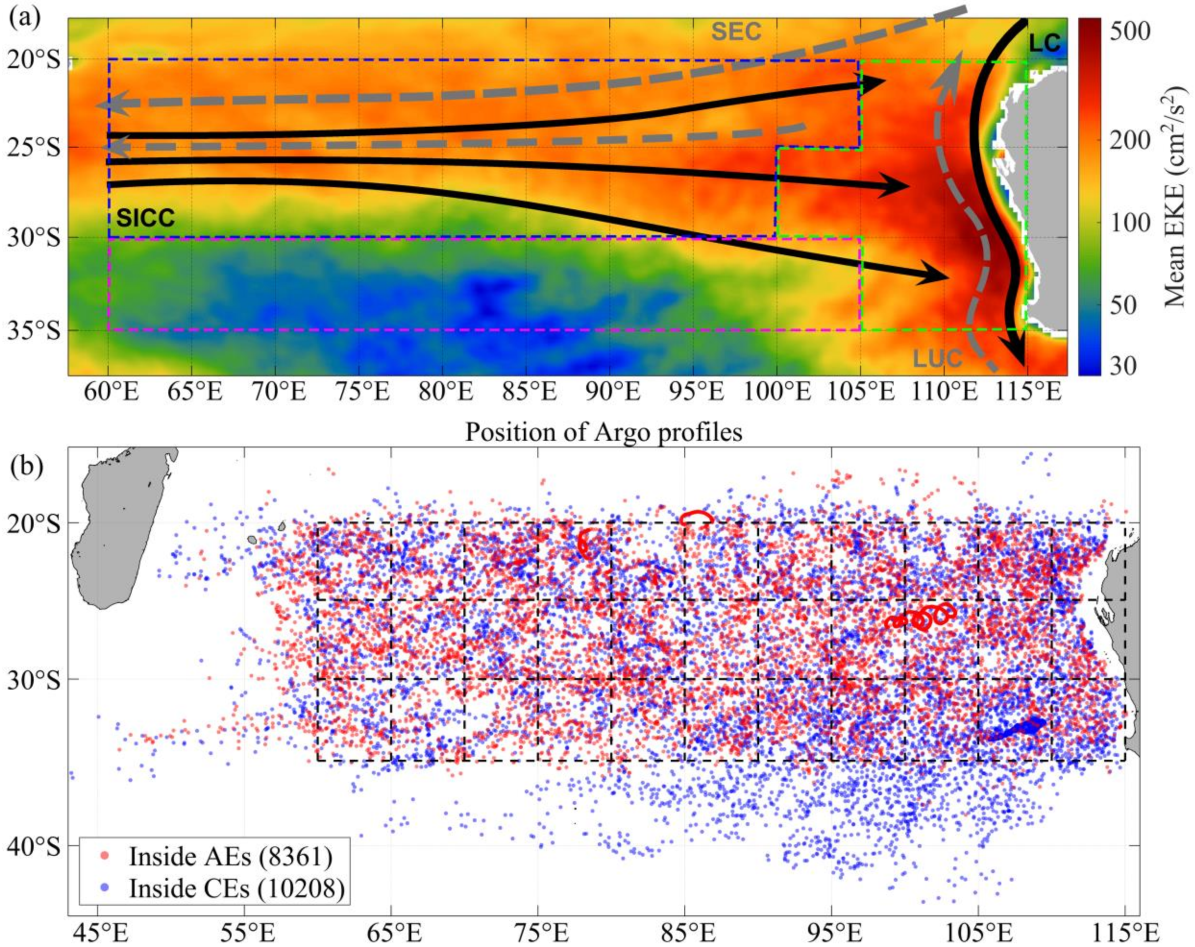

Fig. 1. (a) Climatological mean surface geostrophic EKE (color shading) and major current systems in the SEIO. The climatological mean EKE is calculated from satellite-derived surface geostrophic velocity anomalies for 1993–2018, with details provided in Section 2.1. Thick solid black lines indicate surface currents, whereas thick dashed gray lines indicate subsurface currents. LC: Leeuwin Current; LUC: Leeuwin Undercurrent; SEC: South Equatorial Current; SICC: South Indian Countercurrent. Thick dashed green, blue and magenta lines delineate the LC system (LCS), SICC system (SICCS) and low-EKE regions, respectively. Note that the color scale is logarithmic. (b) Locations of Argo profiles used in this study. Blue dots denote profiles in CEs, whereas red dots denote those in AEs (see Section 2.3 for details on the classification of Argo profiles). Thick dashed black lines delineate the 5°×5° subregions used in this study.

The three-dimensional structures of eddies in the SEIO have been widely investigated through both case studies (Morrow et al., 2003; Feng et al., 2007; Mao et al., 2019) and statistical studies (Dilmahamod et al., 2018; He et al., 2021). By combining satellite observed sea surface height (SSH) data with Argo profiles, previous studies have identified two types of eddies with distinct vertical structures in the SEIO: surface-intensified eddies and subsurface-intensified eddies (Dilmahamod et al., 2018). CEs are predominantly subsurface-intensified, whereas AEs are mainly surface-intensified in the LCS (Feng et al., 2007; Mao et al., 2019; He et al., 2021). The lifespan of the subsurface-intensified eddies is slightly longer than that of the surface-intensified eddies (Dilmahamod et al., 2018). However, the geographic distribution of the subsurface-intensified eddies generation sites in the SEIO remains poorly understood. Furthermore, whether the three-dimensional structures of CEs and AEs differ in the open ocean is still unclear.

CEs in the LCS region tend to have significantly longer lifespans than AEs, whereas such a difference is not evident for eddies in the SICCS region (Zhang et al., 2020). Several factors have been proposed to explain why CEs in the LCS have longer lifespans, including their larger relative vorticity magnitude and stronger nonlinearity (Zhang et al., 2020), as well as their deeper vertical extent and greater volume-integrated energy (He et al., 2021). In contrast, outside the LCS region, the lifespans of CEs and AEs become comparable, raising the question of whether this reduced lifespan contrast is associated with a convergence in their vertical structures.

The main objective of this study is to investigate the spatial distribution of the three-dimensional structures of SEIO eddies and to examine the relationships among their vertical structure, energy, and lifespan. We adopt and slightly refine the reconstruction method proposed by He et al. (2021), which separates background and eddy-induced contributions to density anomalies observed by Argo floats, and enables the composite analysis of eddy structures over relatively small regions (see Section 2 and Appendix A for details). Using this method, we analyze regional variations in eddy vertical structure, calculate the eddy volume-integrated energy in each subregion, and assess their relationships with eddy lifespan.

The remainder of the paper is organized as follows: Section 2 describes the data and methods. Section 3 analyzes the spatial distributions of eddy surface properties, vertical structure, and energy. Section 4 discusses the influence of energy dissipation on eddy lifespan. Section 5 summarizes the key findings.

2 Data and methods

2.1 Altimetry, eddy and Argo profiles data

The satellite observational sea level anomaly (SLA) and surface geostrophic velocity anomalies are obtained from the Copernicus Marine Environment Monitoring Service (https://marine.copernicus.eu/). These data are daily sampled with a spatial resolution of 0.25°×0.25°. We used “all sat merged” data from January 1993 to December 2018. The surface eddy kinetic energy (EKE) is estimated by

$$EKE_{sur} = \frac{{u'_g}^2 + {v'_g}^2}{2}, \quad (1)$$

where u'_g and v'_g are the surface geostrophic velocity anomalies obtained by applying a 270-day high-pass Butterworth filter.

The daily altimetric Mesoscale Eddy Trajectories Atlas product (META3.1exp DT allsat) from January 1993 to December 2018 are based on the absolute dynamic topography (ADT) product from Archiving, Validation, and Interpretation of Satellite Oceanographic (AVISO). The detection algorithm is based on *py-eddy-tracker* (PET) algorithm of Mason et al. (2014).The eddy tracking procedure is based on the overlap of outermost closed contour, in which eddies are linked if the overlap ratio between their outermost contours exceeds 5%. To address the issue of “missing eddies,” the tracking algorithm searches for a potential matching eddy over a period of up to 5 days (Pegliasco et al., 2022). The dataset contains a daily time series of central position, polarity, radius, amplitude, and perimeter coordinates of each eddy.

Delayed-mode Argo data profiles from January 2000 to December 2018 provide available temperature and salinity data from the surface to ~2000 m. These profiles have been automatically preprocessed and quality controlled by the Argo data center. Following previous studies (Chaigneau et al., 2011; Yang et al., 2013), only the Argo profile data meeting the following standards are used for further analyses:

1. The quality flag of pressure, temperature and salinity data are good or probably good (i.e., Argo quality flag 1 or 2);
2. The vertical spacing between two consecutive sampling levels within a single Argo profile should not exceed a given limit (Δz) (i.e., Δz = 25 m for the 0-100 m layer, Δz = 50 m for the 100-300 m layer, Δz =100m for the 300-1000 m layer);
3. Each profile should have no less than 30 data points.

Note that the dense clusters of blue or red dots in the 105°–110°E, 35°–30°S and 100°–105°E, 30°–20°S boxes are from two Argo floats that profiled to a shallow depth of ~300 m, resulting in more frequent surfacings. These floats were also analyzed in Mao et al. (2019).

The selected Argo profiles were then linearly interpolated onto 150 regularly spaced vertical levels every 10 m from 10 m to 1500 m depth. Then we calculate the density from the temperature and salinity of Argo profiles, and then subtract the climatological density of WOA2018 (Boyer et al., 2018) to obtain the Argo density anomaly ρ'_{Argo}.

2.2 Statistics of eddy properties

In the following, the term "eddy realization" refers to a snapshot of an eddy on a specific day, while the term "eddy" encompasses all snapshots of the eddy throughout its lifecycle. The lifespan of each eddy is defined as the time from the first day the eddy is identified to the last day it is tracked. The amplitude is defined as the height difference between the extremum of SLA within the eddy and the SLA around the eddy perimeter. The eddy radius is defined as the radius of a circle with an area equal to that within the eddy perimeter.

For each eddy, the characteristic amplitude and radius are computed by averaging the amplitude and radius during its mature stage, which is defined as the period spanning from 25% to 75% of the eddy's lifespan.

Based on these definitions, regional statistics are derived as follows: The mean lifespan of CEs (AEs) in each subregion (Fig. 2a) is calculated by averaging the lifespans of all CEs (AEs) that originate within that subregion. Similarly, the regional mean amplitude and regional mean radius of CEs (AEs) are computed by averaging the characteristic amplitude and radius, respectively, of all CEs (AEs) originating in each subregion.

2.3 Three-dimensional structure of composite eddies

Because satellite SSH data provide continuous coverage across both time and space, while subsurface observations (e.g., Argo profiles) are spatially and temporally sparse, reconstructing eddy structures using only subsurface data can lead to biases influenced by the observation location and eddy amplitude. Our primary approach to reconstructing the eddy three-dimensional structure involves decomposing the SSH field into background and eddy-induced components, establishing a relationship between these two SSH fields and subsurface density anomalies, and then projecting SSH onto the density anomaly field within the eddy. Based on this, we compute the corresponding geostrophic current velocity.

In this study, we construct the three-dimensional structure of CEs and AEs in each 5°×5° subregion (Fig. 1b). It should be noted that the three-dimensional structure of eddies in a given subregion, as described in this study, refers to the average structure of eddies originating in that region, rather than the average structure of eddy realizations (an instantaneous snapshot of an eddy at a specific time) located in the region. This is because eddies tend to maintain their vertical structure for a long distance (Pegliasco et al., 2015; Text S1, Figs. S1 and S2 in the supplemental material). For each subregion (outlined by dashed boxes in Fig. 1b), the three-dimensional structures of CEs and AEs are constructed separately following the procedure described below.

1. Identify all quality-controlled Argo profiles located within CEs/AEs generated in the region: For each CE/AE realization, check if there are Argo profiles from the same calendar day (UTC) located within the CE/AE perimeter. If so, the Argo profile is considered to be located within the CE/AE.
2. Calculate the eddy-induced and background SSH anomaly (SSHA) at the location and time of the Argo profiles: In He et al. (2021), η'_{bg} was defined as the eddy edge height, which can vary markedly during eddy evolution due to merging and splitting. Here η'_{bg} is obtained by applying a 270-day low-pass filter to satellite-observed SLA η', providing a more stable representation of the background current. The eddy-induced component is then defined as $\eta'_{eddy} = \eta' - \eta'_{bg}$. Finally, both η'_{bg} and η'_{eddy} are linearly interpolated to the time and location of each Argo profile.
3. Calculate the eddy density coefficients and vertical mode $H(z)$: The eddy-induced (α) and background (β) density coefficients, along with the offset term (C) are estimated using least-square fitting method (see detailed derivations in Appendix A):
$$\rho'_{Argo}(z) = \alpha(z) \cdot \eta'_{eddy} + \beta(z) \cdot \eta'_{bg} + C(z). \tag{2}$$
The dimensionless eddy vertical mode $H(z)$ is expressed by $H(z) = -\frac{1}{\rho_0}\int_{z_{ref}}^{z} \alpha(z)dz'$, where ρ_0 is the reference seawater density 1034 kg/m^3 and z_{ref} is the reference depth -1500 m. By definition, *H(z)* starts from 0 at z_{ref} and increases or decreases toward the surface depending on whether the density anomaly has the same or opposite sign as the eddy polarity (i.e., positive for CEs and negative for AEs). *H(z)* represents the ratio of geostrophic velocity at depth *z* relative to the surface, thereby describing the vertical structure of the eddy-induced velocity (see item 5).
4. Construct the eddy-induced and background SSHA of regional composite CE/AE (η'_{eddy} and η'_{bg}) and the corresponding eddy-induced surface geostrophic velocity anomaly (u'_g and v'_g): First, for CEs/AEs originating in the region, we select each eddy realization in the eddy's mature stage, along with the η'_{bg} and η'_{eddy} around the eddy. Next, we transform the η'_{bg} and η'_{eddy} of these CE/AE realizations to an eddy-centered coordinator system. The origin is placed at the position of the minimal/maximal SSHA in the eddy and the horizontal coordinates are normalized by eddy radius. Then, we average the transformed η'_{bg} and η'_{eddy} over CEs and AEs realizations separately to obtain the CE and AE composites for each subregion. Finally, using the composite η'_{eddy} and the regional

mean radius (Fig. 2c) of CEs/AEs, u_g' and v_g', are calculated based on the geostrophic relationship (see Figs. S3 and S4 in the supplemental material).

5. Reconstruct the three-dimensional structure of density $\widehat{\rho'}$ and eddy-induced velocity, $\widehat{u'}$ and $\widehat{v'}$, of the regional average CE/AE as follows:

$$\widehat{\rho'}(x,y,z) = \alpha(z) \cdot \eta'_{eddy}(x,y) + \beta(z) \cdot \eta'_{bg}(x,y) + C(z), \tag{3}$$

$$\widehat{u'}(x,y,z) = H(z) \cdot u_g'(x,y), \tag{4a}$$

$$\widehat{v'}(x,y,z) = H(z) \cdot v_g'(x,y). \tag{4b}$$

Here, the superscript hat (^) denotes reconstructed physical quantities. $\widehat{u'}$ and $\widehat{v'}$ can be derived from the eddy-induced density anomaly, $\widehat{\rho'}_{eddy} = \alpha(z) \cdot \eta'_{eddy}(x,y)$, via thermal wind relation. However, in this study, we directly compute these velocities using *H(z)*, which is derived from the pressure anomaly using the geostrophic relationship (see Eqs. A14a and A14b in Appendix A for details). These two approaches are mathematically equivalent.

In 1993-2016, the number of eddies generated in each subregion ranges from 715 to 1354, including 38519 to 120089 eddy realizations. The highest number of eddy realizations occurs in the LCS region (Fig. 1a), where the eddy lifespans are the longest. The number of Argo profiles used to calculate the eddy density coefficients in each subregion ranges from 230 to 2303. Similarly, due to the longer eddy lifespan, the eastern boundary region has more profiles used for calculating the coefficients. It is important to note that the selected Argo profiles cover the entire lifecycle of the eddies, not just the mature stage.

To quantify the correlations between eddy lifespan and vertical structure, an eddy vertical scale,

$$D = \int_{z_{ref}}^{0} H(z)dz, \tag{5}$$

is defined.

2.4 Eddy energy

Based on the reconstructed density and velocity fields of the regionally average eddy, the EKE and EPE are given by:

$$K_e = \frac{1}{2}\rho_0\left(\widehat{u'}^2 + \widehat{v'}^2\right) = \frac{1}{2}\rho_0\left(\widehat{u_g'}^2 + \widehat{v_g'}^2\right)H^2, \tag{6}$$

$$P_e = \frac{1}{2}\frac{g^2}{\rho_0 N^2}\widehat{\rho'_{eddy}}^2 = \frac{1}{2}\frac{g^2}{\rho_0} \cdot \frac{\alpha^2 {\eta'_{eddy}}^2}{N^2} \tag{7}$$

where *g* is the gravity acceleration 9.8 m/s^2, *N* is the buoyancy frequency, $\widehat{\rho'_{eddy}} = \alpha \cdot \eta'_{eddy}$ is the eddy-induced density anomalies.

The area-integrated EKE ($K(z)$) and EPE ($P(z)$) of the regional mean eddy are calculated by:

$$K(z) = \int_0^{2\pi} d\theta \int_0^R K_e \cdot rdr, \quad (8)$$

$$P(z) = \int_0^{2\pi} d\theta \int_0^R P_e \cdot rdr, \quad (9)$$

where r is the radial distance from the eddy center, and R is the regional mean eddy radius, which is assumed to be constant throughout the water column.

The volume-integrated EKE ($\mathcal{K}$) and EPE ($\mathcal{P}$) are calculated by:

$$\mathcal{K} = \int_{z_{ref}}^0 K(z) \cdot dz, \quad (10)$$

$$\mathcal{P} = \int_{z_{ref}}^0 P(z) \cdot dz. \quad (11)$$

3 Eddy properties from observational data

3.1 Eddy surface properties

The spatial distribution of eddy lifespan in the SEIO (Fig. 2a) has a distinct feature that the lifespans of CEs originated in ~10° longitude zone near the eastern boundary are significantly longer than that of other eddies, i.e., AEs originated in the same region or eddies in the open ocean. Specifically, the mean lifespan of CEs originated in the eastern-most subregions is more than 97 days, while that of the other eddies is about 60 days (Fig. 2a).

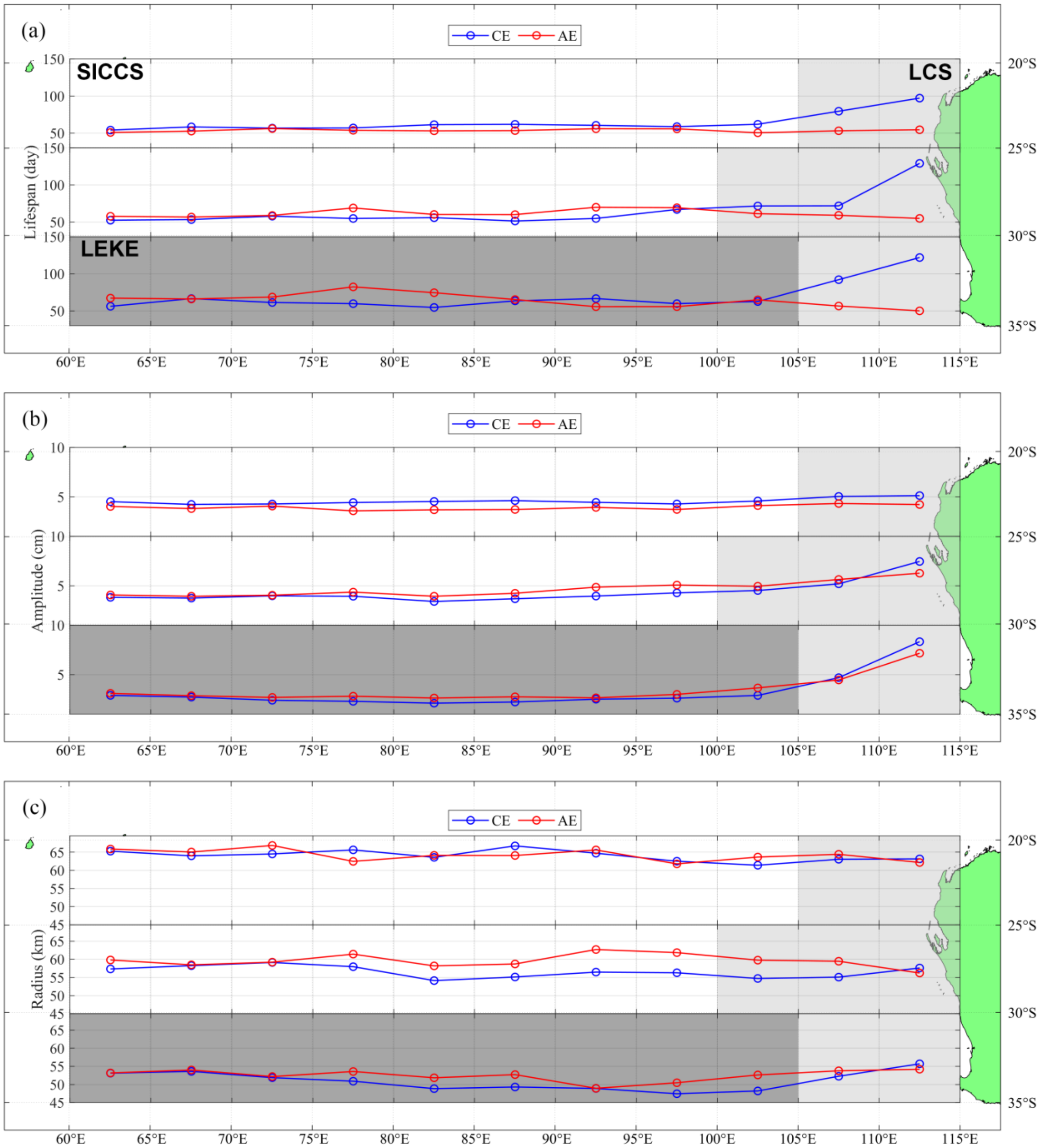

Fig. 2. Spatial variation of eddy (a) lifespan (unit: day), (b) amplitude (unit: cm) and (c) radius (unit: km) in the SEIO. Blue circles denote CEs, and red circles denote AEs. Light shading, the unshaded area and dark gray shading denote LCS, SICCS and low-EKE (LEKE) regions, respectively. The statistical methods for these properties are described in Section 2.2.

The spatial distribution of the eddy amplitude in the SEIO (Fig. 2b) is generally consistent with the surface EKE (Fig. 1a). Since surface EKE and eddy amplitude are naturally highly correlated, the eddies in the LCS region (eastern boundary region) exhibit the highest surface EKE and amplitude, followed by the SICCS region (the open ocean between 30°S and 20°S), while the lowest values are observed in the low-EKE region (the open ocean between 35°S and 30°S).

The eddy radius (Fig. 2c) generally decreases with increasing latitude, which is consistent with the meridional variation of the deformation radius of the first baroclinic mode (Chelton et al., 1998). The mean eddy radii in the three latitude bands of 35°S-30°S, 30°S-25°S and 25°S-20°S are about 52, 58 and 64 km, respectively. Unlike the eddy amplitude and surface EKE, the eddy radius does not exhibit a systematic change in the east-west direction.

In the SICCS region, the eddy lifespan is correlated well with the eddy amplitude, with a correlation coefficient (CC) of 0.73. Specifically, in 25°S-20°S, the amplitude of CEs is higher than that of AEs, and the lifespan of CEs is also longer than that of AEs. In 30°S-25°S, the amplitude of CEs is slightly lower than that of AEs, and the lifespan of CEs in each subregion is generally shorter than that of AEs. But near the eastern boundary, this correlation becomes less linear. In 110°E-115°E, the lifespan of CEs is about twice that of AEs (Fig. 2a), while the amplitude of CEs is only slightly larger—by less than 20%—than that of AEs (Fig. 2b). Additionally, in the low-EKE region, the correlation weakens further, suggesting that other factors significantly influence eddy lifespans in this region.

3.2 Eddy vertical structure

Figs. 3 and 4 show west–east cross slices of the reconstructed eddy three-dimensional structure. Based on the depth of extreme values in geostrophic velocity (Fig. 3), CEs can be broadly classified into two types: surface-intensified and subsurface-intensified eddies. Surface-intensified CEs are are mainly distributed in the LCS north of 25° S, the SICCS and parts of low-EKE region. Their key characteristics include the density anomaly peak (eddy density core) located at depth shallower than 200 m, with intermediate layer density anomalies being relatively small (<0.1 kg/m^3), and velocity peaking near the surface. Subsurface-intensified CEs are mostly distributed in the LCS region (within 10° off the eastern boundary) and the low-EKE region. Their most prominent feature is the density core at intermediate depth ~750 m with density anomalies >0.1 kg/m^3 (Fig. 3a). Additionally, the density anomalies of these eddies are typically negative in the subsurface layer (~100–250 m) and positive at intermediate depths (~400–1400 m), indicating a downward displacement of subsurface water and an upward displacement of intermediate water within the CEs. The maximum velocity occur at subsurface depths of 200-300 m, rather than near the surface (Fig. 3b).

Unlike CEs, AEs are predominantly surface-intensified. Their main characteristics include generally negative density anomalies (Fig. 4a), with the density core located in the subsurface layer (100-200 m), and maximum velocity near the surface (Fig. 4b). In a few subregions, AEs exhibit subsurface-intensified features (e.g., subregions of 110°E-115°E, 30°S-25°S; 85°E-95°E, 35°S-30°S), where positive density anomalies occur near the surface, although they are barely visible in Fig. 4a. However, unlike subsurface-intensified CEs, these AEs have limited impact on density and velocity under intermediate depth. According to the thermal wind balance, the vertical profile of horizontal velocity is determined by the vertical integration of horizontal density gradient. In these AEs, the density anomalies and their gradients are weak below 400 m (Fig. 4a), resulting in correspondingly weak velocities at those depths.

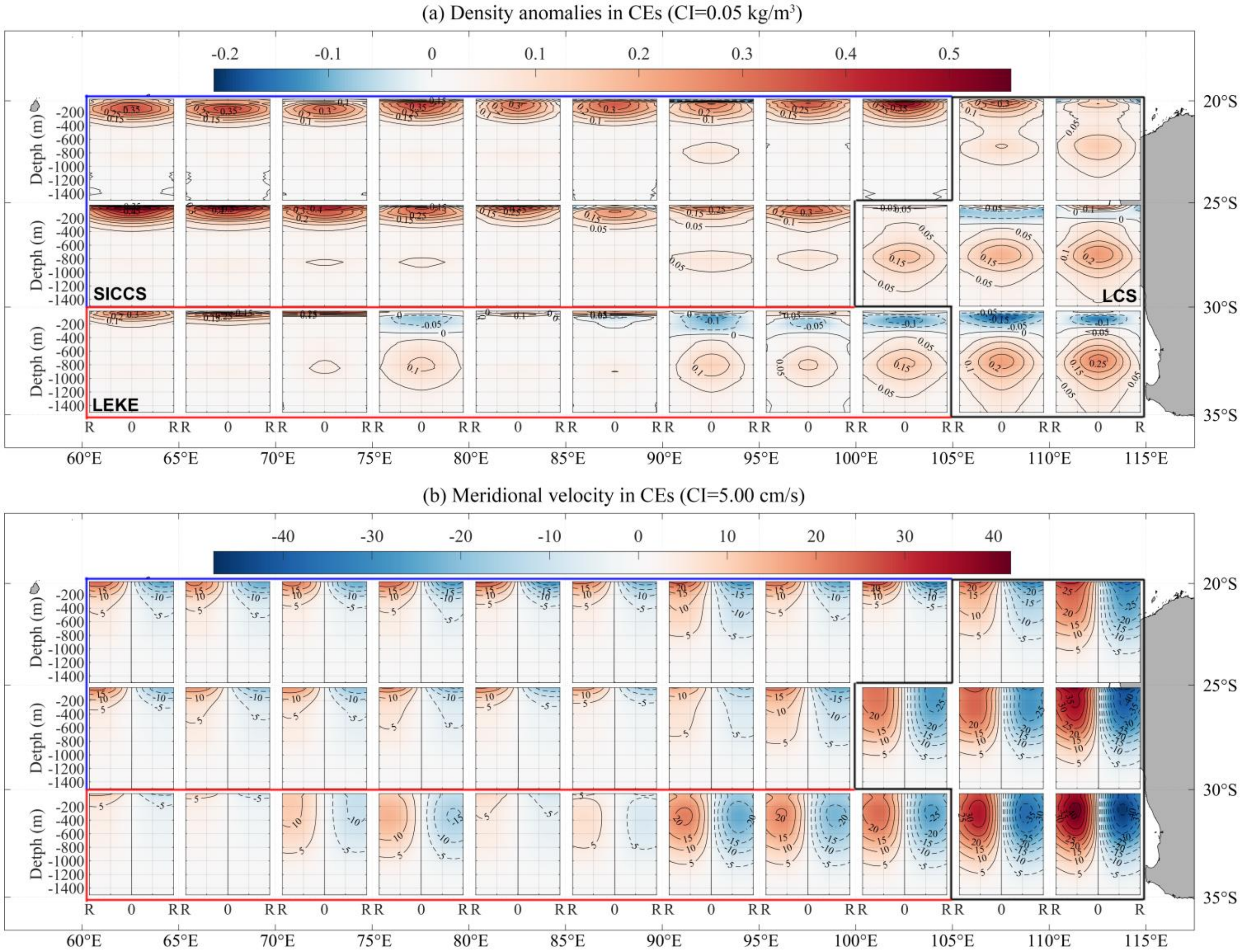

Fig. 3. (a) Density anomalies (unit: kg/m^3) and (b) Meridional component of eddy-induced velocities (unit: cm/s) in CEs in each subregion of the SEIO. The SEIO is divided into the LCS, SICCS, and low-EKE regions, marked by black, blue, and red lines, respectively.

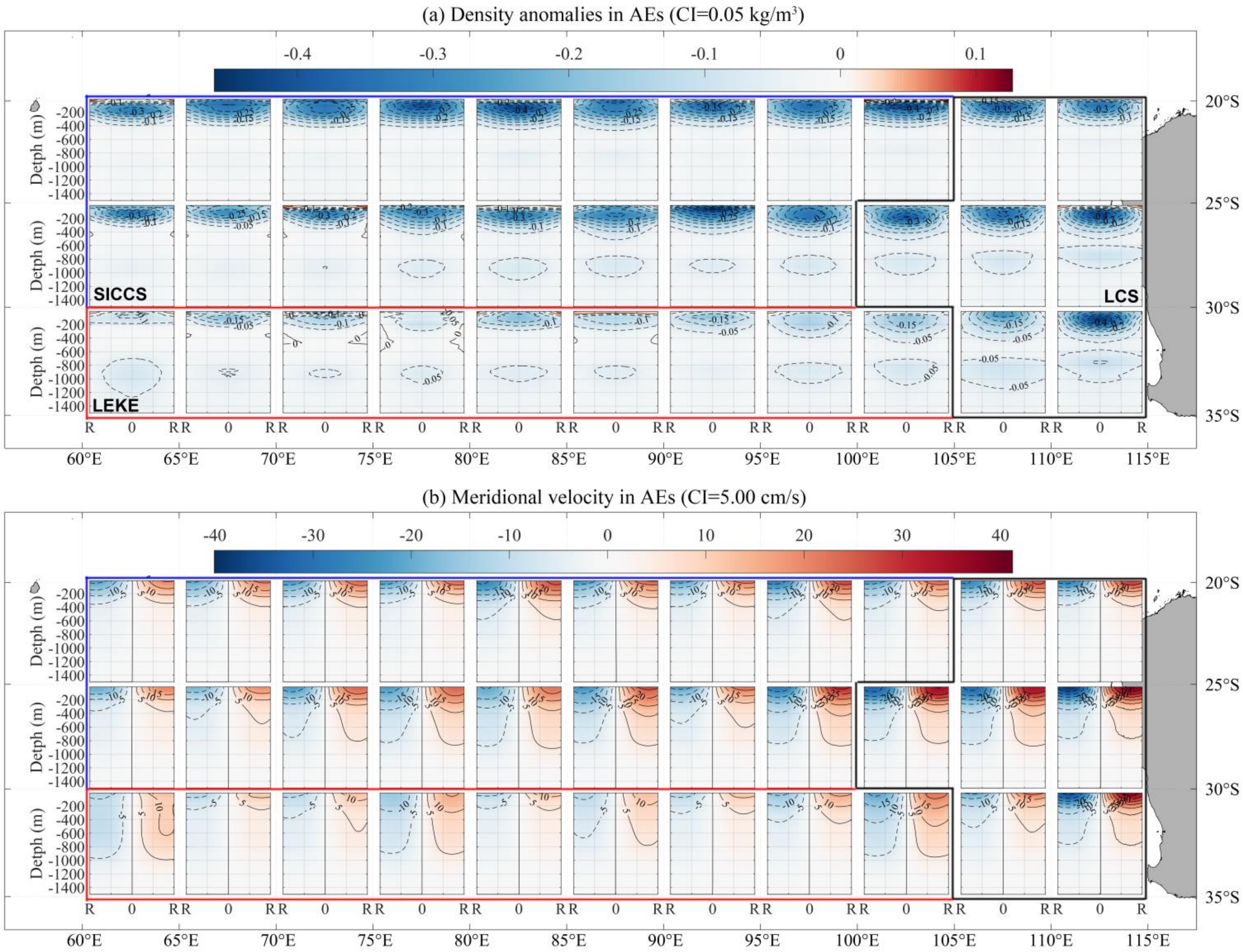

Fig. 4. Same as Fig. 3 but for AEs.

In the LCS region, the numerical simulation by Rennie et al. (2007) also showed that the eddy field is dominated by AEs at the surface and CEs in the intermediate layer. They suggested that the interaction between LC and LUC promotes the generation of eddies with these two distinct vertical structures. The directions of the mean flows in the upper and lower layers might determine the polarity of the subsurface eddies. For instance, in the Peru-Chile Current and California Current systems, where the upper layer mean current is equatorward and the lower layer current is poleward (opposite to that in the LCS), subsurface eddies are predominantly anticyclonic (Chaigneau et al., 2011; Kurian et al., 2011; Pegliasco et al., 2015).

Fig. 3 shows that subsurface-intensified CEs are more prevalent at higher latitudes. In detail, subsurface-intensified CEs in the 25°S-20°S range are confined to a narrow 5° longitudinal band close to the eastern boundary (110°E-115°E). In contrast, those in the 35°S-30°S range have a much broader distribution, covering a 25° longitudinal band off the eastern boundary (90°E-115°E) and a subregion in the open ocean (75°E-80°E). In addition, the density anomalies of AEs at higher latitudes exhibit a pronounced secondary peak in the intermediate layer (400-1000 m), beneath the Subantarctic Mode Water (Fig. 4a). This may be due to weaker density stratification in higher latitudes, which facilitates eddies to extend deeper and develop larger density anomalies (Liu et al., 2020). An independent analysis using reanalysis data (GLORYS12v1) confirms a similar spatial distribution of three-dimensional eddy structures (see Supporting Information Text S2 and Fig. S5).

Fig. 5 shows that the subsurface-intensified eddies have a deeper vertical scale, D (Eq. 5), than the surface-intensified eddies in the LCS. As suggested by Gaube et al. (2015) that eddies with deeper vertical scale have longer lifespan, this relationship holds in the LCS, where CEs have a deeper vertical scale and a longer lifespan than AEs. However, in the low-EKE region, the vertical scale of some CEs can be over 1000 m, but their lifespan has little difference from the other eddies with a shallow vertical scale (Fig. 2a). Therefore, eddy vertical structure alone is insufficient to fully explain eddy lifespan variability in this region, although it remains an important contributing factor.

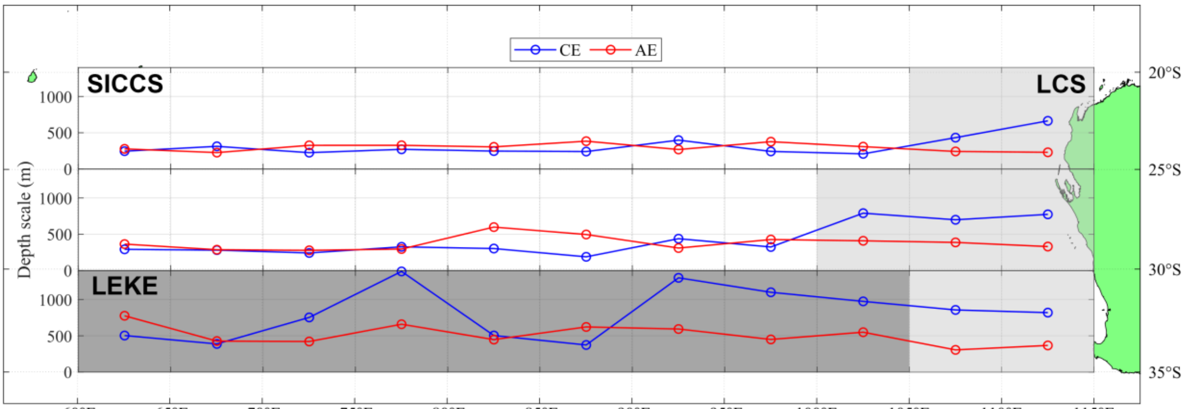

Fig. 5. Spatial variation of eddy vertical scale *D* (see Eq. (5); unit: m). Blue circles denote CEs, and red circles denote AEs. Light shading, no shading and heave gray shading denote LCS, SICCS and low-EKE (LEKE) region, respectively.

3.3 Eddy energy

Vertical profiles of area-integrated EKE (*K(z)*, Fig. 6) can be divided into two types (i.e., surface-intensified and subsurface-intensified). The *K(z)* of surface-intensified eddies (e.g., all AEs and CEs in the SICCS) is the strongest at the surface and weakens rapidly downwards. It drops to 10% of the surface value at an average depth of 450 m. By contrast, the *K(z)* of subsurface-intensified eddies (e.g., CEs in the LCS) is the strongest in the subsurface and drops to 10% of the surface value at an average depth of 970 m.

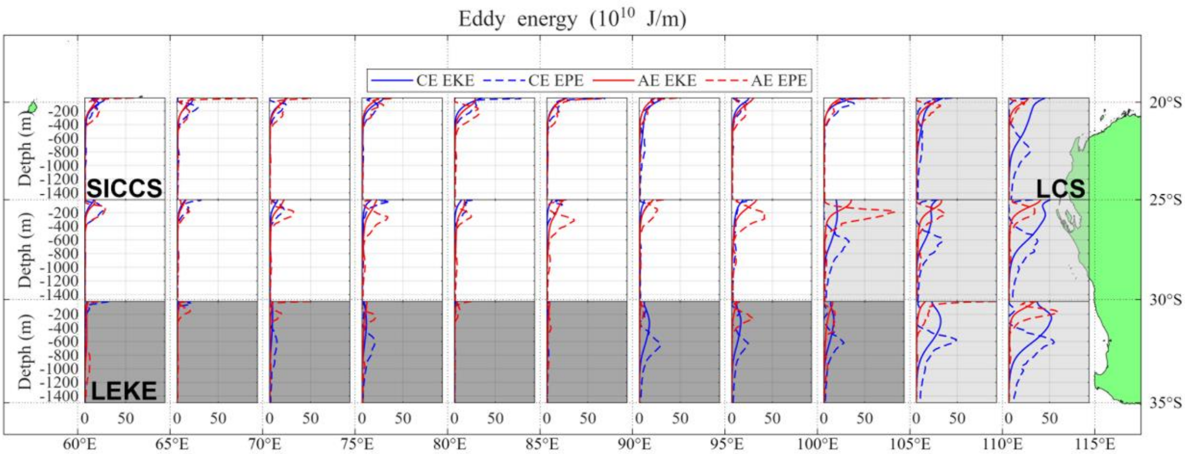

Fig. 6. Vertical profiles of area-integrated EKE (solid lines, unit: J) and EPE (dashed lines, unit: J) of CEs (blue lines) and AEs (red lines) in each subregion of the SEIO. Light shading, the unshaded area and heavy gray shading denote LCS, SICCS and low-EKE (LEKE) regions, respectively.

There are also significant differences in the vertical profiles of the area-integrated EPE between surface-intensified and subsurface-intensified eddies (*P(z)*, Fig.6). The maximum *P(z)* of the surface-intensified eddies occurs near the surface (e.g., AEs in 105°-110°E, 35°S-30°S) or in water depths of 100-300 m (e.g., AEs in 110°-115°E, 35°S-30°S), while the maximum *P(z)* of the subsurface-intensified CEs occurs in a depth of ~650 m. The main reason for this structure is that the maximum eddy-induced density anomalies of two types of eddies occur at different depths. Moreover, the averaged depth of the maximum *P(z)* in the surface-intensified AEs (~200 m) is slightly deeper than that in the surface-intensified CEs (~120 m). Due to the uplift and depression of the isopycnals in the CEs and AEs, respectively, the depths of density cores of CEs and AEs are deeper and shallower (Fig. 5) as well as the depths of the maximum EPE.

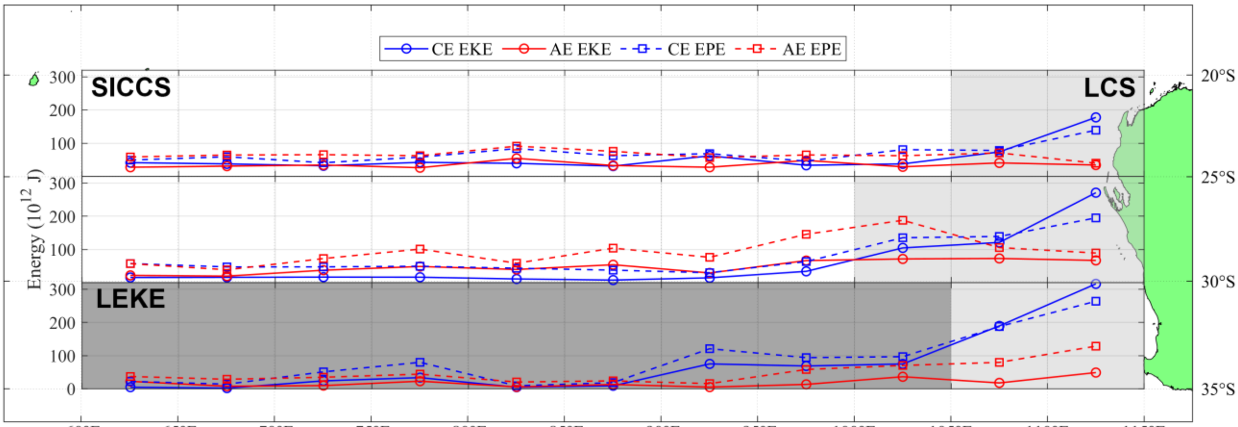

Fig. 7. Spatial variation of volume-integrated EKE (cycles, unit: J) and EPE (squares, unit: J) in the SEIO. Blue markers denote CEs, and red markers denote AEs. Light shading, the unshaded area and heave gray shading denote LCS, SICCS and low-EKE (LEKE) regions, respectively.

Fig. 7 shows the spatial distribution of volume-integrated EKE ($\mathcal{K}$) and EPE ($\mathcal{P}$) of regional composite eddies. Similar to the spatial pattern of surface EKE (Fig. 1a), the $\mathcal{K}$ and $\mathcal{P}$ in the LCS region is much larger than that in the open ocean (Fig. 7). Moreover, the $\mathcal{K}$ and $\mathcal{P}$ of CEs in the eastern boundary region are significantly higher than those of AEs.

Satellite observations show that the horizontal structure of ocean eddies is well approximated by a Gaussian function (Chelton et al., 2011; Wang et al., 2015). Idealized Gaussian eddies have also been widely used in theoretical and numerical studies to investigate eddy dynamics and energetics (e.g., Early et al., 2011). Based on the energy equations of a Gaussian eddy (Eqs. C10 and C11), there are six factors that determine $\mathcal{K}$ and $\mathcal{P}$. Among them, $\mathcal{K}$ is proportional to A^2, H^2, and f^{-2}, where A is the eddy amplitude, H is the vertical mode as defined by Eq. (A5), and f is the Coriolis parameter; $\mathcal{P}$ is proportional to R^2, A^2, α^2, and N^{-2}, where R is the eddy radius, α is the eddy-induced density coefficient, and N is the buoyancy frequency. Among these parameters, amplitude A and vertical structure—represented by either H or α—affect both $\mathcal{K}$ and $\mathcal{P}$. Since A^2, R^2, and f^2 vary only with horizontal position, they determine only the horizontal spatial distribution of eddy energy. In contrast, H^2, α^2, and N^2 are functions of both horizontal position and depth, which means they also influence the vertical structure of eddy energy, as described in Eqs. (C8) and (C9).

To evaluate the influence of each factor on the spatial distribution of eddy volume-integrated energy, we employed a correlation analysis. The results show that the amplitude factor A^2 has the strongest correlation with $\mathcal{K}$ (CC=0.75, Fig. 8a), followed by the vertical mode factor $\int_{z_{ref}}^{0} H^2 dz$ (CC=0.48, Fig. 8b). In contrast, the Coriolis force factor $1/f^2$ exhibits no significant correlation (CC=0.01, not shown). Similarly, the factor correlated the most with $\mathcal{P}$ is also A^2 (Fig. 8c), followed by the vertical displacement factor $\int_{z_{ref}}^{0} \frac{\alpha^2}{N^2} dz$ (Fig. 8d). The radius factor R^2 shows no significant correlation with $\mathcal{P}$ (CC=0.04, not shown). Therefore, the most important factor affecting the spatial variability of eddy energy in the SEIO is the eddy amplitude, followed by the eddy vertical structure.

An intriguing finding is that, according to Eq. (C10), the volume-integrated EKE is independent of eddy radius for a Gaussian eddy. At first glance, this appears counterintuitive, as one might expect that larger eddies would enclose more total EKE. According to the geostrophic relationship, the volume-integrated EKE, $\mathcal{K} \propto U^2 L^2 D \propto A^2 D$, where $U \propto A/L$ is the geostrophic velocity scale, L is the length scale (that is eddy radius), A is the amplitude scale, D is the depth scale of the eddy. When A is held constant, U becomes inversely proportional to L, resulting in $\mathcal{K}$ remaining unchanged. Additionally, the volume-integrated EKE is influenced by eddy's vertical scale. Specifically, eddies with a larger vertical scale typically experience weaker velocity decay with depth, leading to higher volume-integrated EKE.

Similarly, the volume-integrated EPE is also primarily governed by eddy amplitude and vertical scale. Larger amplitudes correspond to stronger eddy-induced density anomalies, ρ'_{eddy}, which, according to Eq. (7), result in greater EPE. Moreover, eddies with deeper vertical extents tend to have density anomalies that extend into deeper layers, where the buoyancy frequency, N, is lower than that in shallower layers, thereby contributing to higher EPE.

Although the above conclusions are derived based on the energy expressions for a Gaussian eddy, the assumption of a Gaussian form is made solely for analytical simplicity. These conclusions are expected to hold more generally and can be extended to eddies with non-Gaussian structures.

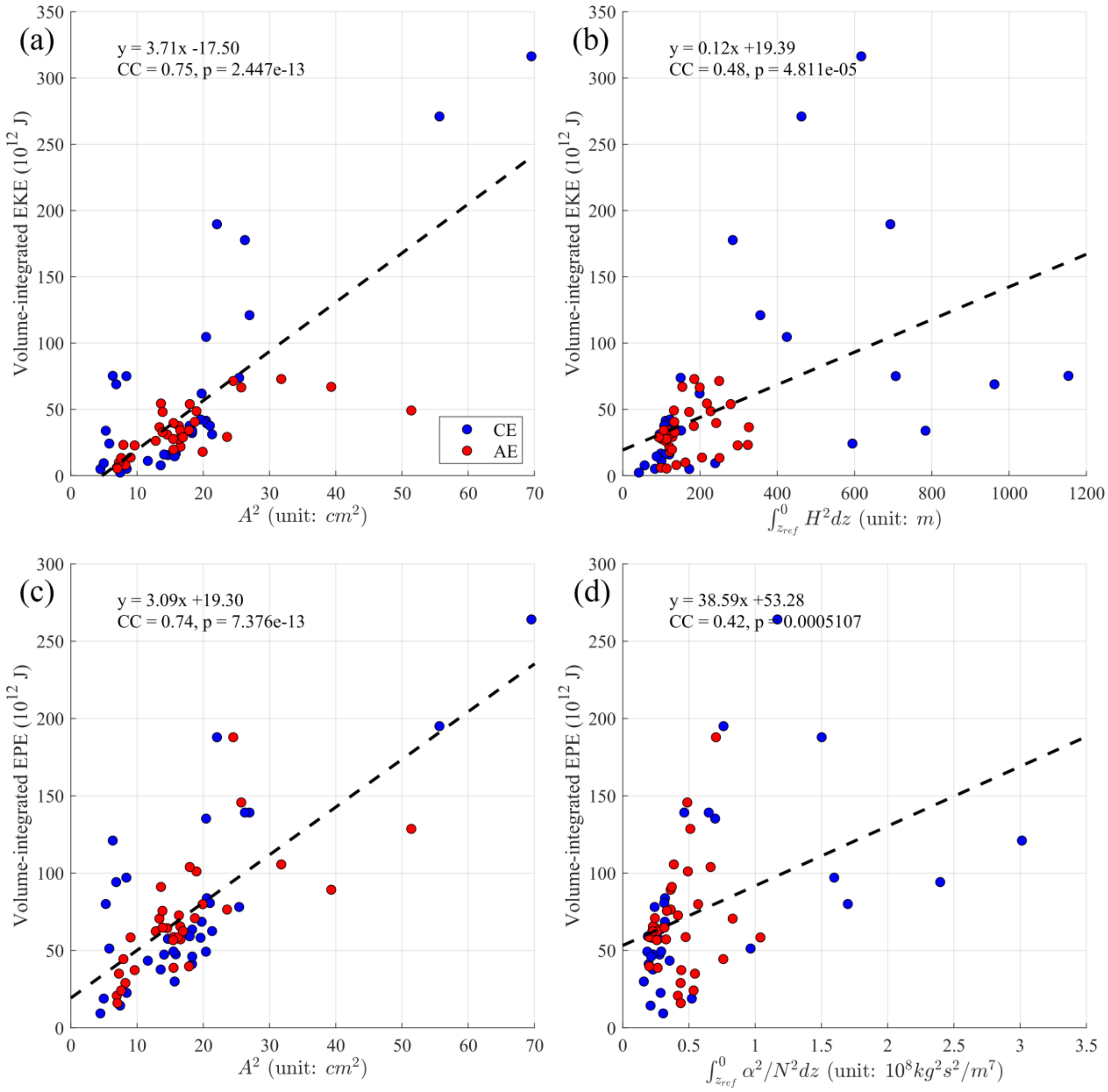

Fig. 8. Scatter plots of eddy amplitude and vertical structure factors vs. volume-integrated EKE ($\mathcal{K}$) and EPE ($\mathcal{P}$). (a) A^2 vs. $\mathcal{K}$; (b) $\int_{z_{ref}}^{0} H^2 dz$ vs. $\mathcal{K}$; (c) A^2 vs. $\mathcal{P}$; (d) $\int_{z_{ref}}^{0} \frac{\alpha^2}{N^2} dz$ vs. $\mathcal{P}$. The red and blue dots denote AEs and CEs, respectively. The dashed lines represent the linear fit results. The linear fit function, correlation coefficient and p-value are displayed in the upper left corner of each plane.

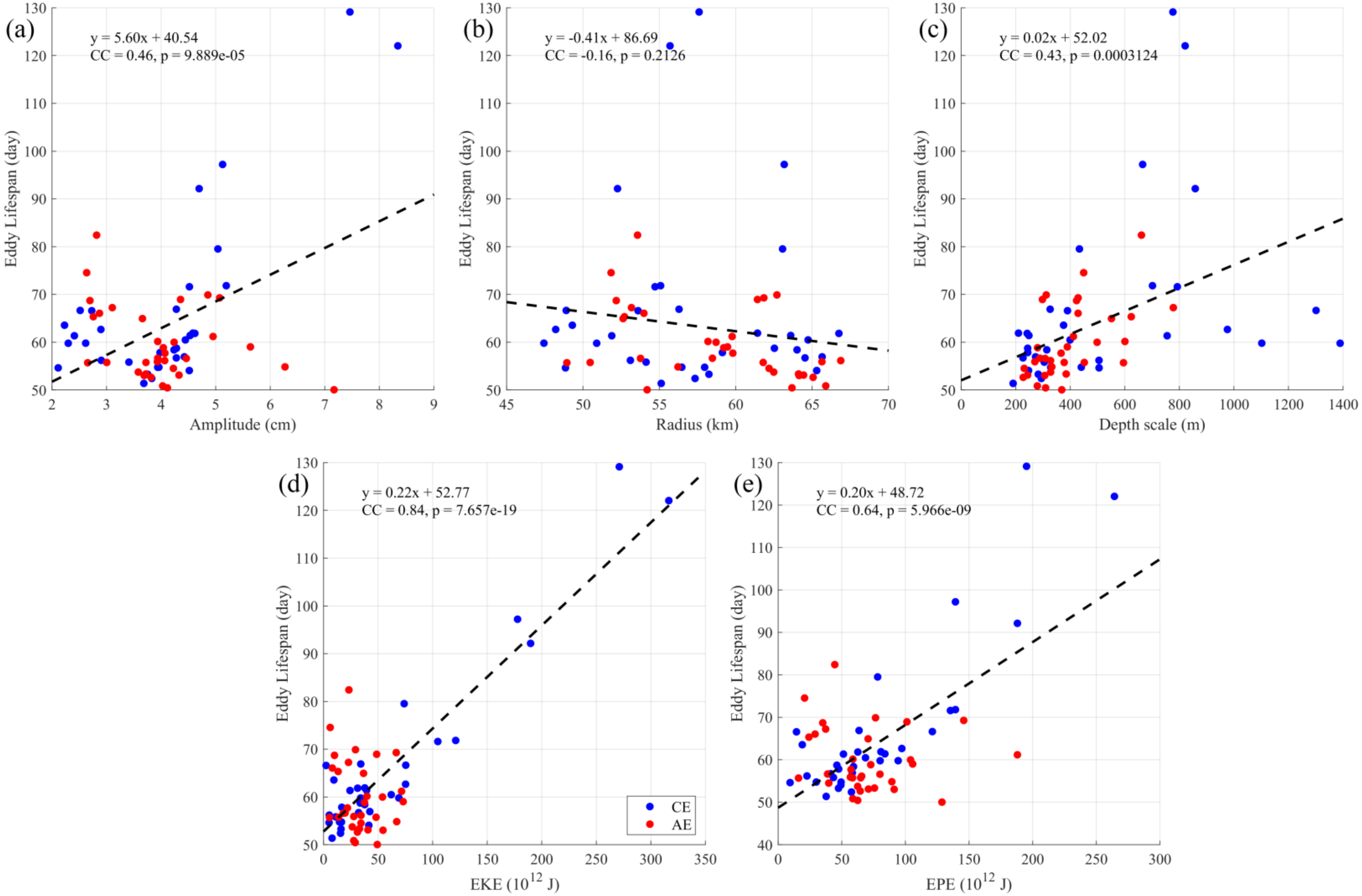

Fig. 9. Scatter plots of eddy lifespan vs. (a) eddy amplitude, (b) radius, (c) depth scale, (d) volume-integrated EKE and (e) EPE. Blue (red) dots denote CEs (AEs). The linear fit function, correlation coefficient and p-value are displayed in the upper left corner of each plane.

Previous studies have indicated that the lifespan of eddies is related to their amplitude, radius, and vertical scale (Chaigneau et al., 2011; Chen et al., 2011; Gaube et al., 2015). We calculated the correlation between the mean eddy lifespan and these three properties, obtaining CCs of 0.46, -0.16, and 0.43, respectively (see Fig. 9a, b, and c). This indicates that the spatial variability of eddy lifespan in the SEIO is influenced by eddy amplitude and vertical scale, but is independent of eddy radius. Furthermore, Fig. 7 shows that the volume-integrated EKE $\mathcal{K}$ and EPE $\mathcal{P}$ have a similar spatial pattern with eddy lifespan in the SEIO. The CC of the eddy lifespan with $\mathcal{K}$ and $\mathcal{P}$ reaches 0.84 (Fig. 9d) and 0.64 (Fig. 9e), respectively, which are significantly higher than that with other properties. This suggests that $\mathcal{K}$ is the factor most closely associated with eddy lifespan.

The strong correlation between eddy lifespan and volume-integrated energy indicates that eddy persistence is essentially controlled by its energy content. If the decay rate is constant and dissipation ends once energy drops below a threshold, higher initial energy naturally prolongs lifespan. As shown in this section, high eddy energy mainly arises from large amplitudes and deep vertical structures. A key question, then, is whether surface- and subsurface-intensified eddies dissipate at the same rate, which will be examined in the next section.

4 Impacts of Eddy structure on energy dissipation

To investigate the impacts of energy dissipation on eddy lifespan, we assume horizontal and vertical Laplacian viscosity for momentum and diffusion for density. In addition, the same horizontal and vertical mixing coefficients (A_h and A_z) are used for both momentum and density. Under these assumptions, and retaining only the dissipative terms in the temporal evolution, the volume-integral EKE and EPE equations take the form:

$$\frac{d\mathcal{K}}{\partial t} = -A_h \varepsilon_h \mathcal{K} - A_z \varepsilon_z \mathcal{K}, \tag{12}$$

$$\frac{d\mathcal{P}}{\partial t} = -A_h \delta_h \mathcal{P} - A_z \delta_z \mathcal{P}, \tag{13}$$

where the damping coefficients are defined as:

$$\varepsilon_z = \frac{2\int \alpha(z)^2 dz}{\rho_0^2 \int H^2(z) dz}, \tag{14}$$

$$\delta_z = \frac{2\int \frac{\left(\frac{d\alpha}{dz}\right)^2}{N^2} dz}{\int \frac{\alpha^2}{N^2} dz}, \tag{15}$$

$$\varepsilon_h = \frac{2 \iint \left\| \nabla_h \boldsymbol{u}_g' \right\|^2 dxdy}{\iint \left| \boldsymbol{u}_g' \right|^2 dxdy}, \tag{16}$$

$$\delta_h = \frac{2 \iint |\nabla_h \eta'|^2 dxdy}{\iint \eta'^2 dxdy}. \tag{17}$$

Here ε_z and δ_z are the vertical damping coefficients of EKE and EPE, respectively, determined by the eddy vertical structure. ε_h and δ_h are the horizontal damping coefficients of EKE and EPE, respectively, determined by the eddy spatial pattern. Introducing energy damping coefficients links dissipation rates directly to the eddies' three-dimensional structure. When eddy structures are stable, these rates can be treated as constants, so Eqs. (12–13) yield analytical solutions. Detailed derivations are provided in Appendix B.

4.1 E-folding time for energy vertical dissipation

To investigate the differences in energy dissipation between eddies of different vertical structures, we analyzed the representative three-dimensional structures of CEs and AEs in the SICCS and LCS, together with their corresponding energy damping rates (Fig. 10). In the SICCS, composite eddies were selected within 80°E–85°E, 30°S–25°S, while in the LCS region they were selected within 110°E–115°E, 30°S–25°S. As shown in Figs. 3–4, among the four representative cases, the CE in the LCS is a typical subsurface-intensified eddy, whereas the other three are surface-intensified. Nevertheless, these surface-intensified eddies exhibit noticeable differences in both horizontal and vertical structures (Fig. 10a–b, d–f), which in turn lead to distinct energy damping rates.

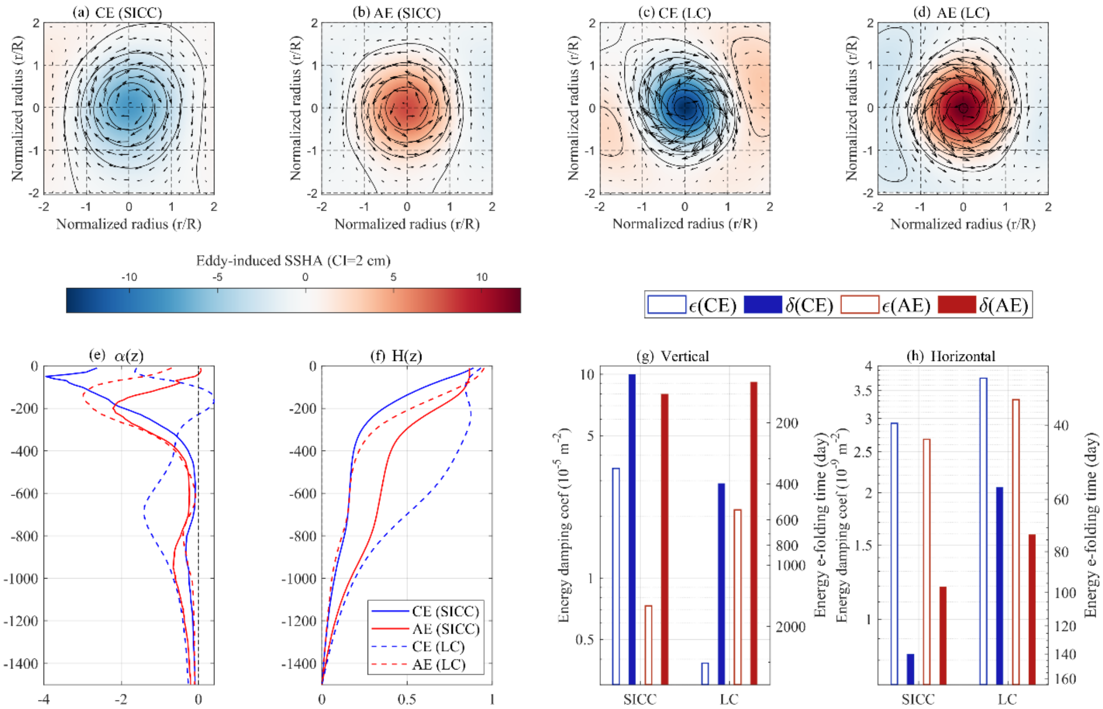

Fig. 10. Typical SEIO eddy structures and energy dissipation coefficients. (a–d) SSHA (color shading and contours, CI = 2 cm) with geostrophic velocity vectors of composite CEs and AEs in the SICCS and LCS (a: CE SICCS; b: AE SICCS; c: CE LCS; d: AE LCS); The *x* and *y* axes denote the zonal and meridional directions, respectively. (e–f) vertical density anomaly coefficient, *α(z)* (e), and eddy vertical mode, *H(z)* (f), for SICCS (solid) and LCS (dashed) eddies; blue/red lines denote CEs/AEs; (g–h) vertical (g) and horizontal (h) damping coefficients (m^{-2}) of EKE (ε) and EPE (δ), with hollow/shaded bars for EKE/EPE and edges colored blue/red for CEs/AEs. Right-hand axes indicate e-folding times (days), calculated with $A_z = 1\times10^{-3}$ m^2s^{-1} for (g) and $A_h = 1\times10^{2}$ m^2s^{-1} for (h).

Fig. 10g shows that δ_z is consistently higher than ε_z, with δ_z being nearly twice as large. This indicates that EPE decays much faster through vertical mixing compared with EKE. Among the four representative eddy types, both δ_z and ε_z of the CE in the LCS are markedly smaller than those of the other three. For the remaining eddies, the damping coefficients follow a clear order: the AE in the SICCS < the AE in the LC < the CE in the SICCS. This hierarchy is consistent with their density core depths (Fig. 10e), suggesting that eddies with deeper vertical structures are associated with smaller vertical energy damping coefficients.

Fig. 10g also presents the e-folding times of eddy energy ($T_e = 1/(A_z\epsilon_z)$ for EKE and $T_e = 1/(A_z\delta_z)$ for EPE), assuming a vertical mixing coefficient A_z=1×10^{-3} m^{2}s^{-1}. The e-folding times of EPE for the four eddies range from 116 to 398 days (filled bars in Fig. 10g), which is several times longer than the typical eddy lifespan. Notably, the decay time of the subsurface-intensified eddy is approximately three times that of the surface-intensified eddies. This implies that under vertical-mixing-dominated dissipation, subsurface-intensified eddies are expected to persist much longer than their surface-intensified counterparts.

In the global oceans, the mean eddy vertical mixing coefficient A_z is on the order of 10^{-4} m^{2}s^{-1} (Wunch and Ferrari, 2004). In the open ocean, A_z is typically around 10^{-5} m^{2}s^{-1}, while near steep topography it can reach 10^{-3} m^{2}s^{-1} or higher. Thus, the above e-folding time estimates adopt an upper-limit value of A_z, which is applicable only to regions near steep topography or with frequent internal wave activity. Previous studies have shown that in marginal seas and western boundary regions, eddy–topography interactions make vertical mixing the dominant pathway of eddy energy dissipation (Nikurashin et al., 2012; Gula et al., 2016). By contrast, in most open-ocean regions, the contribution of vertical mixing to eddy energy dissipation is likely to be minor.

4.2 E-folding time for energy horizontal dissipation

Fig. 10h shows the horizontal damping coefficients of the four eddies. In contrast to vertical damping, the horizontal damping coefficient of EKE (ε_h) is higher than that of EPE (δ_h), with ε_h roughly twice δ_h, indicating that horizontal mixing leads to faster EKE decay. Among the four eddy types, both δ_h and ε_h are largest for the LCS CE, likely because its horizontal pattern is less axisymmetric, forming an elliptical shape oriented northwest-southeast rather than the nearly circular pattern of the other three eddies.

The horizontal mixing coefficient in the ocean varies with the scale of motion. The altimeter data used in this study have a spatial resolution of 1/4°, which is approximately 25 km. Previous tracer release experiments (Okubo, 1971; Ledwell et al., 1998) and analyses based on Lagrangian drifters and floats (Lumpkin et al., 2002; Qian et al., 2013) suggest that the eddy horizontal mixing coefficient A_h typically ranges from 10^2 to 10^4 m^{2}s^{-1}, at a characteristic length scale of 10^4 m (Huang, 2014).

Setting A_h=1×10^2 m^{2}s^{-1}, the e-folding times of EKE for the four eddies range from 31 to 43 days (hollow bars in Fig. 10h), a variation much smaller than that due to vertical mixing. We next use these estimates to evaluate the eddy lifespan when horizontal mixing dominates eddy energy dissipation.

When horizontal mixing dominates, Eq. (12) reduces to

$$\frac{d\mathcal{K}}{dt} = -A_h \varepsilon_h \mathcal{K}. \tag{13}$$

The solution to Eq. (13) is

$$\mathcal{K}(t) = E_0 e^{-A_h \varepsilon_h t}, \tag{14}$$

where E_0 is the peak eddy kinetic energy. An eddy is considered extinct when its kinetic energy decreases to a prescribed extinction threshold, denoted by E_1. The time required for the eddy kinetic energy to decay from E_0 to E_1 is therefore

$$T_d = \frac{1}{A_h \varepsilon_h} ln\left(\frac{E_0}{E_1}\right). \tag{15}$$

In the LCS region, the total EKE of the composite AE is ~67 TJ. We take 67/*e* TJ as a common effective extinction threshold for both AEs and CEs , where *e* is the base of the natural logarithm.. The e-folding time, $1/(A_h \varepsilon_h)$, of the AE is ~35 days (Fig. 10h). Substituting these values into Eq. (15) gives

$$T_{AE} = 2 \times 35 \times ln\left(\frac{67}{67/e}\right) \approx 70\ days. \tag{16}$$

The total EKE of the composite CE is ~271 TJ, about 4 times that of the AE. Using the same effective extinction threshold and the CE e-folding time of ~31 days (Fig. 10h), we obtain

$$T_{CE} = 2 \times 31 \times ln\left(\frac{271}{67/e}\right) \approx 148\ days. \tag{17}$$

These estimated lifespans are reasonably close to the mean lifespans derived from eddy tracking, which are 129 days for CEs and 59 days for AEs in the LCS region (Fig. 2a). This agreement suggests that the differences in initial eddy energy and horizontal dissipation rate can largely explain the contrasting lifespans of CEs and AEs in this region.

It should be noted that the value of A_h used here is close to its lower limit; when A_h is larger, the corresponding e-folding time will be shorter. In addition, since the horizontal dissipation rate of EPE is slower than that of EKE, energy conversion from EPE to EKE can occur during the dissipation process, which tends to slow down the overall rate of EKE decay.

By comparing the e-folding times of eddy energy associated with vertical and horizontal mixing, we suggest that horizontal mixing likely exerts a more significant influence on the evolution of SEIO eddies. CEs in the LCS, owing to their higher volume-integrated energy, can sustain a longer lifespan even under relatively strong horizontal dissipation. In addition, subsurface-intensified eddies exhibit considerably slower energy decay from vertical mixing compared with surface-intensified eddies.

5 Conclusions

Using the satellite observations and Argo floats data, this study investigates geographical distribution of the eddy vertical structures and energy in the SEIO and explores their relationship with eddy lifespan. Composite analyses reveal that the spatial distribution of eddy vertical structures is primarily associated with mean current systems and latitude. Notably, the vertical structure of CEs varies significantly across different subregions, while the structure of AEs shows less variation. The surface-intensified CEs mainly originate from the SICCS, whose density core is at a depth of ~70 m, and subsurface-intensified CEs mainly originate from the LCS (~10° longitude off the eastern boundary) and the open ocean south of 30°S, whose density core and maximum velocity are at depths of ~750 m and ~290 m, respectively. The surface-intensified AEs widely originate from the entire region of SEIO, whose density core is at a depth of ~110 m, while the sources of subsurface-intensified AEs are only scattered in a few regions, whose density core and maximum velocity are at depths of ~160 m and ~80 m, respectively. The regional differences in the vertical structures of CEs and AEs indicate that eddy vertical structure is not solely controlled by background stratification, as traditionally assumed (Zhang et al., 2013), but is also strongly influenced by the characteristics of the mean flow.

Previous studies have primarily related eddy lifespan to surface EKE (Chen and Han, 2019); however, surface EKE does not necessarily represent the magnitude of the total (volume-integrated) energy owing to variations in eddy vertical structure. This study shows that the eddy lifespan in the SEIO is significantly correlated with the volume-integrated EKE, and the correlation coefficient reaches 0.84. The spatial variability of eddy energy is mainly controlled by eddy amplitude and eddy vertical structure, whereas the effects of eddy radius and the Coriolis parameter are negligible.

Finaly, we examine the contrasting energy dissipation of surface- and subsurface-intensified eddies and its implications for lifespan. The eddy energy dissipation term is expressed as a function of eddy structure, allowing us to quantify regional differences in energy decay rates among eddies with distinct vertical structures, and provide corresponding quantitative estimates. The results reveal that, subsurface-intensified eddies experience much weaker vertical mixing than their surface-intensified counterparts, while horizontal mixing dominates energy dissipation in the SEIO and varies little among the four eddy types. Vertical mixing dissipates EPE faster than EKE, whereas horizontal mixing shows the opposite tendency.

In summary, this study emphasizes the important role of eddy three-dimensional structure in regulating eddy energetics, dissipation, and lifespan, beyond what can be inferred from surface properties alone. Our analysis primarily focuses on the role of energy dissipation in shaping eddy longevity. However, other processes may also contribute to eddy energetics. Previous studies have shown that atmospheric wind forcing can perform substantial work on ocean eddies (Xu et al., 2016), and that baroclinic and barotropic energy conversions, pressure work, and dissipation play important roles in the eddy energy budget in the SEIO, particularly in the LCS region (Zhang et al., 2020). How these processes operate on, and potentially differ between, surface- and subsurface-intensified eddies remains an open question that warrants further investigation.

Several limitations should be acknowledged. The three-dimensional eddy structures reconstructed here are derived from satellite and Argo observations and therefore represent composite mean characteristics rather than the full types of structures exhibited by individual eddies. In addition, estimates of energy dissipation rely on parameterized mixing coefficients and composite eddy structures, which may introduce uncertainties in the magnitude of dissipation rates. Despite these limitations, the relative contrasts between surface- and subsurface-intensified eddies are robust across subregions and datasets, supporting the main conclusions of this study.

More broadly, our results suggest that commonly used assumptions of similar vertical structures for CEs and AEs may lead to biases in estimates of eddy-induced transport and energy dissipation. Incorporating vertical structural diversity, particularly the contrast between surface- and subsurface-intensified eddies, into eddy parameterization schemes may improve the representation of mesoscale processes in ocean circulation and climate models. These findings further motivate future observational and high-resolution modeling studies to explicitly account for eddy vertical structure when assessing eddy impacts across different oceanic regions.

APPENDIX A

Reconstruction of eddy vertical structure

According to the different dynamic mechanisms that cause SSH variation, firstly we decompose the SSH η as follows:

$$\eta = \overline{\eta} + \eta' = \overline{\eta} + \eta'_{bg} + \eta'_{eddy}, \tag{A1}$$

Where $\overline{\eta}$ is climatological mean SSH, η' is the SSH deviation from $\overline{\eta}$, which is composed of background SSHA η'_{bg}, and eddy-induced SSHA η'_{eddy}. η'_{bg} is induced by background circulation, which has low frequency variations such as seasonal or interannual variations, while η'_{eddy} is induced by eddies with high frequency variations. Thus, we use a lowpass filter of 270 days on η' to get η'_{bg}, then calculate η'_{eddy} by $\eta' - \eta'_{bg}$.

Similarly, the density can also be decomposed as above:

$$\rho = \overline{\rho} + \rho' = \overline{\rho} + \rho'_{bg} + \rho'_{eddy}, \tag{A2}$$

where $\overline{\rho}$ is the climatological mean perturbation density, ρ' is density anomaly, which is composed of background density anomaly ρ'_{bg} and eddy-induced part ρ'_{eddy}. $\overline{\rho}$ can be calculated from a climatological dataset, such as WOA2018. However, since the Argo profile is scattered, it's not feasible to directly obtain the ρ'_{bg} and ρ'_{eddy} through temporal filtering. Thus, we discuss the relationship between SSHA and density anomalies, and then calculate ρ'_{eddy} from η'_{eddy}.

Mesoscale motions are typically in quasi-geostrophic and hydrostatic balance (Cushman-Roisin and Beckers, 2011). The eddy pressure anomaly p'_{eddy}, the density anomaly ρ'_{eddy}, and eddy-induced velocity u' and v' can be expressed as:

$$\rho'_{eddy}(x, y, z, t) = -\frac{1}{g} \cdot \frac{\partial p'_{eddy}(x,y,z,t)}{\partial z}, \tag{A3}$$

$$u'(x, y, z, t) = -\frac{1}{\rho_0 f_0} \cdot \frac{\partial p'_{eddy}(x,y,z,t)}{\partial y}, \tag{A4a}$$

$$v'(x, y, z, t) = \frac{1}{\rho_0 f_0} \cdot \frac{\partial p'_{eddy}(x,y,z,t)}{\partial x}, \tag{A4b}$$

where g is the gravitation acceleration, ρ_0 is the reference seawater density, and f_0 is the Coriolis parameter.

Assume that p'_{eddy} can be separated into a horizontal pattern $P(x, y, t)$ and a vertical mode $H(z)$, such that

$$p'_{eddy}(x, y, z, t) = P(x, y, t) \cdot H(z). \tag{A5}$$

At the sea surface ($z = 0$), we have

$$p'_{eddy}(x, y, 0, t) \approx \rho_0 g \eta'_{eddy} = P(x, y, t) H(0), \tag{A6}$$

where the approximation $p'_{eddy} \approx -g \int_0^z \rho'_{eddy}\, dz + \rho_0 g \eta'_{eddy}$ is derived in detail in supporting information text S3.

By setting the normalization $H(0) = 1$, we obtain

$$P(x,y,t) = \rho_0 g \eta'_{eddy}. \tag{A7}$$

Substituting Eqs. (A5) and (A7) into Eq. (A3) yields:

$$\rho'_{eddy}(x,y,z,t) = \alpha(z) \cdot \eta'_{eddy}(x,y,t), \tag{A8}$$

where,

$$\alpha(z) = -\rho_0 \cdot \frac{\partial H(z)}{\partial z}. \tag{A9}$$

This coefficient establishes the relationship between ρ'_{eddy} and η'_{eddy}, so we refer to $\alpha(z)$ as the eddy-induced density coefficient. Similarly, we can express ρ'_{bg} as a linear function of η'_{bg},

$$\rho'_{bg}(x,y,z,t) = \beta(z) \cdot \eta'_{bg}(x,y,t), \tag{A10}$$

and $\beta(z)$ is referred to as the background density coefficient. Substituting Eqs. (A8) to (A10) into Eq. (A2) and adding an error term ε, we obtain:

$$\rho'(x,y,z,t) = \alpha(z) \cdot \eta'_{eddy}(x,y,t) + \beta(z) \cdot \eta'_{bg}(x,y,t) + \varepsilon(x,y,z,t). \tag{A11}$$

Because both eddies and background currents can have multiple vertical structure types, the coefficients $\alpha(z)$ and $\beta(z)$ represent the mean vertical structures.

For each Argo profile, a ρ' profile can be obtained. η'_{eddy} and η'_{bg} can be deduced from the Satellite observational SSHA, while $\alpha(z)$ and $\beta(z)$ remain unknown, which can be calculated by least squares fitting. Since the means of ρ', η'_{eddy} and η'_{bg} are not necessarily be zero, we introduce an additional offset term $C(z)$ to eliminate biases in the regression model:

$$\rho' = \alpha(z) \cdot \eta'_{eddy} + \beta(z) \cdot \eta'_{bg} + C(z) + \varepsilon. \tag{A12}$$

Once $\alpha(z)$ is obtained, $H(z)$ can be calculated using Eq. (A9). Although we assumed $H(0) = 1$, the density anomalies in the near-surface mixed layer are influenced by various factors, such as surface heating and cooling, precipitation, and the mixing effects of eddy rotation on sea surface temperature. These factors can introduce significant error in the calculated $\alpha(z)$. Therefore, we use integration from a reference depth upwards to calculate $H(z)$:

$$H(z) = -\frac{1}{\rho_0} \int_{z_{ref}}^{z} \alpha(z) dz, \tag{A13}$$

where $z_{ref} = -1500\ m$ is the reference depth.

Substituting Eqs. (A5) and (A7) into Eqs. (A4a) and (A4b), the eddy-induced velocity can be expressed as:

$$u' = u'_g \cdot H(z), \tag{A14a}$$

$$v' = v'_g \cdot H(z). \tag{A14b}$$

where $u_g' = -\frac{g}{f_0} \cdot \frac{\partial \eta'}{\partial y}$ and $v_g' = \frac{g}{f_0} \cdot \frac{\partial \eta'}{\partial x}$ represent the surface geostrophic velocity.

APPENDIX B

Eddy energy damping coefficients

1. Friction terms for energy equations

To derive the equations for EKE and EPE, we start from the momentum equations and density equation:

$$\frac{\partial u}{\partial t} + \boldsymbol{u} \cdot \nabla u - fv = -\frac{1}{\rho_0}\frac{\partial p}{\partial x} + \mathcal{D}_u, \tag{B1a}$$

$$\frac{\partial v}{\partial t} + \boldsymbol{u} \cdot \nabla v + fu = -\frac{1}{\rho_0}\frac{\partial p}{\partial y} + \mathcal{D}_v, \tag{B1b}$$

$$\frac{\partial \rho_a}{\partial t} + \boldsymbol{u} \cdot \nabla \rho_a = \frac{\rho_0 N^2}{g} w + \mathcal{D}_\rho, \tag{B1c}$$

where p is the hydrostatic pressure, $\boldsymbol{u} = (u, v, w)$ is the three-dimensional velocity vector, $\nabla = \frac{\partial}{\partial x}\hat{\imath} + \frac{\partial}{\partial y}\hat{\jmath} + \frac{\partial}{\partial z}\hat{k}$ is the three-dimensional Nabla operator. The friction or diffusion terms $\mathcal{D}_u$, $\mathcal{D}_v$ and $\mathcal{D}_\rho$ are defined as:

$$\mathcal{D}_u = \nabla_h \cdot (A_h \nabla_h u) + \frac{\partial}{\partial z}\left(A_z \frac{\partial u}{\partial z}\right), \tag{B2a}$$

$$\mathcal{D}_v = \nabla_h \cdot (A_h \nabla_h v) + \frac{\partial}{\partial z}\left(A_z \frac{\partial v}{\partial z}\right), \tag{B2b}$$

$$\mathcal{D}_\rho = \nabla_h \cdot (A_h \nabla_h \rho_a) + \frac{\partial}{\partial z}\left(A_z \frac{\partial \rho_a}{\partial z}\right), \tag{B2c}$$

where $\nabla_h = \frac{\partial}{\partial x}\hat{\imath} + \frac{\partial}{\partial y}\hat{\jmath}$ is the horizontal gradient operator, A_h and A_z are the horizontal and vertical mixing coefficients, respectively.

Following the derivation of the Lorenz energy cycle for the ocean (von Storch et al., 2012; Chen et al., 2014; Kang et al., 2015; Yan et al., 2023), the governing equations for EKE and EPE can be written as:

$$\begin{aligned}\frac{\partial K_e}{\partial t} = & \underbrace{-\rho_0\left(u'\boldsymbol{u}' \cdot \nabla\overline{u} + v'\boldsymbol{u}' \cdot \nabla\overline{v}\right) + \rho_0\left(u'\nabla \cdot \overline{u'\boldsymbol{u}'} + v'\nabla \cdot \overline{v'\boldsymbol{u}'}\right)}_{BTC} \\ & \underbrace{-g\rho_a'w'}_{C(P_e,K_e)} \underbrace{-\nabla \cdot \left(\boldsymbol{u}K_e\right)}_{ADV_k} - \underbrace{\nabla \cdot \left(\boldsymbol{u}'p'\right)}_{P_k} + \underbrace{\rho_0\left(u'\mathcal{D}_u' + v'\mathcal{D}_v'\right)}_{D_k}\end{aligned}, \tag{B3}$$

$$\frac{\partial P_e}{\partial t} = \underbrace{-\frac{g^2}{\rho_0 N^2}\rho_a' \boldsymbol{u}' \cdot \nabla \overline{\rho_a} + \frac{g^2}{\rho_0 N^2}\rho_a' \nabla \cdot \overline{\boldsymbol{u}'\rho_a'}}_{BCC} \underbrace{+g\rho_a' w'}_{-C(P_e,K_e)} \\ \underbrace{-\nabla \cdot (\boldsymbol{u}P)}_{ADV_p} + \underbrace{\frac{g^2}{\rho_0 N^2}\rho_a' \mathcal{D}_\rho'}_{D_p}, \tag{B4}$$

where $K_e = \frac{1}{2}\rho_0(u'^2 + v'^2)$ is the EKE, $P_e = \frac{g^2 \rho_a'^2}{2\rho_0 N^2}$ is the EPE. The overbar $\overline{(\cdot)}$ denotes a temporal average, which can represent either the long-term climatological mean (as in Appendix A) or a moving average over a specified time window.

The last term in Eq. (B3), $\mathcal{D}_k$, is the friction term for the EKE. Assuming that A_h and A_z are constant, and substituting Eqs. (B2a) and (B2b) into $\mathcal{D}_k$, we obtain

$$D_k = \underbrace{\rho_0 A_h \boldsymbol{u}_h' \cdot \nabla_h^2 \boldsymbol{u}_h'}_{①} + \underbrace{\rho_0 A_z \boldsymbol{u}_h' \cdot \frac{\partial^2 \boldsymbol{u}'}{\partial z^2}}_{②}, \tag{B5}$$

where is $\boldsymbol{u}_h' = (u', v')$ the horizontal perturbation velocity vector. The first term on the right-hand side of Eq. (B5) represents horizontal diffusion/dissipation, which can be express as:

$$① = \rho_0 A_h \boldsymbol{u}_h' \cdot \nabla_h^2 \boldsymbol{u}_h' = \rho_0 A_h \left[\nabla_h^2 \left(\frac{1}{2}|\boldsymbol{u}_h'|^2\right) - \|\nabla_h \boldsymbol{u}_h'\|^2\right], \tag{B6}$$

where $|\boldsymbol{u}_h'|^2 = u'^2 + v'^2$ is the squared norm of vector $\boldsymbol{u}_h'$, and

$$\|\nabla_h \boldsymbol{u}_h'\|^2 = \left(\frac{\partial u'}{\partial x}\right)^2 + \left(\frac{\partial u'}{\partial y}\right)^2 + \left(\frac{\partial v'}{\partial x}\right)^2 + \left(\frac{\partial v'}{\partial y}\right)^2$$

is the squared Frobenius norm of tensor $\nabla_h \boldsymbol{u}_h'$. The second term on the right-hand side of Eq. (B5) represents vertical diffusion/dissipation, which can be express as:

$$② = \rho_0 A_z \boldsymbol{u}_h' \cdot \frac{\partial^2 \boldsymbol{u}_h'}{\partial z^2} = \rho_0 A_z \left[\frac{\partial^2}{\partial z^2}\left(\frac{1}{2}|\boldsymbol{u}_h'|^2\right) - \left|\frac{\partial \boldsymbol{u}_h'}{\partial z}\right|^2\right]. \tag{B7}$$

The last term in Eq. (B4), $\mathcal{D}_p$, is the friction term for the EPE. By using Eq. (B2c), $\mathcal{D}_p$ can be express as:

$$D_p = \underbrace{A_h \frac{g^2}{\rho_0 N^2}\rho_a' \nabla_h^2 \rho_a'}_{③} + \underbrace{A_z \frac{g^2}{\rho_0 N^2}\rho_a' \frac{\partial^2 \rho_a'}{\partial z^2}}_{④}. \tag{B8}$$

The first and second terms in the right hand of Eq. (B8) are the horizontal and vertical friction terms, respectively, which can be expressed as:

$$③ = A_h \frac{g^2}{\rho_0 N^2} \rho_a' \nabla_h^2 \rho_a' = A_h \frac{g^2}{\rho_0 N^2} \left[\nabla_h^2 \left(\frac{1}{2} {\rho_a'}^2 \right) - |\nabla_h \rho_a'|^2 \right], \tag{B9}$$

$$④ = A_z \frac{g^2}{\rho_0 N^2} \rho_a' \frac{\partial^2 \rho_a'}{\partial z^2} = A_z \frac{g^2}{\rho_0 N^2} \left[\frac{\partial^2}{\partial z^2} \left(\frac{1}{2} {\rho_a'}^2 \right) - \left(\frac{\partial \rho_a'}{\partial z} \right)^2 \right]. \tag{B10}$$

2. Damping coefficients for eddy energy

Since our focus is on the impact of energy dissipation on the eddy lifespan, the following derivation considers only the contribution of the friction terms to the eddy energy budget. By integrating Eq. (B3) over the eddy volume and retaining only the temporal tendency and friction terms, we obtain:

$$\frac{d\mathcal{K}}{dt} = -A_h \varepsilon_h \mathcal{K} - A_z \varepsilon_z \mathcal{K}, \tag{B11}$$

where

$$\mathcal{K} = \iiint K_e dV = \frac{1}{2} \rho_0 \iiint |\boldsymbol{u}_h'|^2 dV, \tag{B12}$$

is the volume-integral EKE,

$$\varepsilon_h = -\frac{1}{\mathcal{K} A_h} \iiint ① dV = -\frac{2 \iiint \left[\nabla_h^2 \left(\frac{1}{2} |\boldsymbol{u}_h'|^2 \right) - \|\nabla_h \boldsymbol{u}_h'\|^2 \right] dV}{\iiint |\boldsymbol{u}_h'|^2 dV}, \tag{B13}$$

is referred to as the horizontal damping coefficient of EKE,

$$\varepsilon_z = -\frac{1}{\mathcal{K} A_z} \iiint ② dV = -\frac{2 \iiint \left[\frac{\partial^2}{\partial z^2} \left(\frac{1}{2} |\boldsymbol{u}_h'|^2 \right) - \left(\frac{\partial \boldsymbol{u}_h'}{\partial z} \right)^2 \right] dV}{\iiint |\boldsymbol{u}_h'|^2 dV}, \tag{B14}$$

is referred to as the vertical damping coefficient of EKE. When ε_h and ε_z are time-invariant, the solution of Eq. (B11) is $\mathcal{K} = Ce^{-(A_h \varepsilon_h + A_z \varepsilon_z)t}$, thus the e-folding time of $\mathcal{K}$ is $\frac{1}{A_h \varepsilon_h + A_z \varepsilon_z}$.

Similarly, by integrating Eq. (B4) over the eddy volume and retaining only the temporal tendency and friction terms, we obtain:

$$\frac{d\mathcal{P}}{dt} = -A_h \delta_h \mathcal{P} - A_z \delta_z \mathcal{P}, \tag{B15}$$

where

$$\mathcal{P} = \iiint P_e dV = \frac{g^2}{2\rho_0} \iiint {\rho_a'}^2 dV, \tag{B16}$$

is the volume-integral EPE,

$$\delta_h = -\frac{1}{\mathcal{P} A_h} \iiint ③ dV = -\frac{2 \iiint \left[\nabla_h^2 \left(\frac{1}{2} {\rho_a'}^2 \right) - |\nabla_h \rho_a'|^2 \right] dV}{\iiint {\rho_a'}^2 dV}, \tag{B17}$$

is referred to as the horizontal damping coefficient of EPE,

$$\delta_z = -\frac{1}{\mathcal{K}A_z}\iiint ④ dV = -\frac{2\iiint\left[\frac{\partial^2}{\partial z^2}\left(\frac{1}{2}{\rho'_a}^2\right)-\left(\frac{\partial \rho'_a}{\partial z}\right)^2\right]dV}{\iiint {\rho'_a}^2 dV}, \quad \text{(B18)}$$

is referred to as the vertical damping coefficient of EPE. When δ_h and δ_z are time-invariant, the solution of Eq. (B15) is $\mathcal{P} = Ce^{-(A_h\delta_h+A_z\delta_z)t}$, thus the e-folding time of $\mathcal{P}$ is $\frac{1}{A_h\delta_h+A_z\delta_z}$.

In this study, the eddy structure is decomposed into a horizontal pattern and a vertical mode, as described by Eq. A5. By substituting Eqs. (A14a) and (A14b) into Eqs. (B13) and (B14), the horizontal and vertical damping coefficients of EKE can be expressed as:

$$\varepsilon_h = -\left[\frac{\iint \nabla_h^2\left(\left|\boldsymbol{u}'_g\right|^2\right)dxdy - 2\iint\left\|\nabla_h \boldsymbol{u}'_g\right\|^2 dxdy}{\iint\left|\boldsymbol{u}'_g\right|^2 dxdy}\right],$$

and

$$\varepsilon_z = -\left[\frac{\int\frac{\partial^2 H(z)^2}{\partial z^2}dz - 2\int\left(\frac{\partial H(z)}{\partial z}\right)^2 dz}{\int H^2(z)dz}\right],$$

where $\boldsymbol{u}'_g$ is the surface geostrophic velocity (u'_g, v'_g).

According to Gauss's theorem, the first term in the numerator of ε_h can be expressed as: $\iint \nabla_h^2\left(\left|\boldsymbol{u}'_g\right|^2\right)dxdy = \oint \vec{n}\cdot\nabla_h\left(\left|\boldsymbol{u}'_g\right|^2\right)dl$, where $\vec{n}$ denotes the outward normal vector of the eddy boundary. This term represents the diffusion of EKE across the eddy boundary. The second term in the numerator, $\iint\left\|\nabla_h \boldsymbol{u}'_g\right\|^2 dxdy$, is positive definite and represents the horizontal dissipation of EKE within the eddy. Since the EKE diffusion term acts similar to the dissipation term but typically contributes less to the total energy decay (Figure now shown), we retain only the dominant dissipation term in our formulation. Thus, ε_h is given by $\varepsilon_h = \frac{2\iint\left\|\nabla_h \boldsymbol{u}'_g\right\|^2 dxdy}{\iint\left|\boldsymbol{u}'_g\right|^2 dxdy}$.

Similarly, the first term in the numerator of ε_z, $\int\frac{\partial^2 H(z)^2}{\partial z^2}dz = \left.\frac{\partial H(z)}{\partial z}\right|_{-h}^{0}$, represents the wind work and bottom friction exerted on the eddy. The second term in the numerator: $\int\left(\frac{\partial H(z)}{\partial z}\right)^2 dz$, is positive definite and represents the vertical dissipation. Since vertical shear vanishes at the reference depth, the contribution from bottom friction can be neglected. At the sea surface, uncertainties in the reconstructed eddy structure are relatively large (He et al., 2021), making reliable estimation of wind work difficult. Therefore, we also consider only the dissipation term in the main text, given by: $\varepsilon_z = \frac{2\int \alpha(z)^2 dz}{\rho_0^2\int H^2(z)dz}$.

By substituting Eq. (A8) into Eqs. (B17) and (B18), the horizontal and vertical damping coefficients of EPE can be expressed as: $\delta_h = -\left[\frac{\iint \nabla_h^2(\eta'^2)dxdy - 2\iint |\nabla_h \eta'|^2 dxdy}{\iint \eta'^2 dxdy}\right]$, and

$$\delta_z = -\left[\frac{\int \frac{\left(\frac{d^2\alpha^2}{dz^2}\right)}{N^2}dz - 2\int \frac{\left(\frac{d\alpha}{dz}\right)^2}{N^2}dz}{\int \frac{\alpha^2}{N^2}dz}\right].$$

The first term in the numerator of both δ_h and δ_z is not positive definite, representing the diffusion effects on the eddy's lateral and vertical boundaries, respectively. The second term in each case is positive definite, representing the EPE dissipation due to horizontal and vertical mixing. Similarly, we consider only the EPE dissipation term in the text, that is, $\delta_h = \frac{2\iint |\nabla_h \eta'|^2 dxdy}{\iint \eta'^2 dxdy}$, and $\delta_z = \frac{2\int \frac{\left(\frac{d\alpha}{dz}\right)^2}{N^2}dz}{\int \frac{\alpha^2}{N^2}dz}$.

APPENDIX C

Energy for an idealized Gaussian eddy

The eddy-induced SSHA, η', for an idealized Gaussian eddy is given by:

$$\eta'(r) = Ae^{-\frac{r^2}{R^2}}, \tag{C1}$$

where A is eddy amplitude (positive for the AE and negative for the CE), R is eddy radius, *r* is the radial distance from eddy center, *e* is the base of the natural logarithm. According to the geostrophic relationship in cylindrical coordinate:

$$-fu'_{\theta g} = -g\frac{\partial \eta'}{\partial r}, \tag{C2}$$

$$fu'_{rg} = -\frac{g}{r}\frac{\partial \eta'}{\partial \theta}, \tag{C3}$$

where $u'_{\theta g}$ and u'_{rg} are the azimuthal and radial velocities at the sea surface, respectively. From the above two equations, it can be derived that:

$$u'_{\theta g} = -\frac{2g}{f}\cdot\frac{r}{R^2}\cdot\eta'(r), \tag{C4}$$

$$u'_{rg} = 0. \tag{C5}$$

Similar to Eq. (A5), we decompose the eddy motion into a product of a horizontal pattern and a vertical mode, then the eddy-induced density anomaly ρ' and velocity are:

$$\rho'(x,y,z) = \alpha(z)\cdot\eta'(x,y), \tag{C6}$$

$$u'_\theta(x,y,z) = u'_{\theta g}(r) \cdot H(z), \tag{C7}$$

where $\alpha(z)$ is eddy-induced density coefficient, $H(z)$ is eddy vertical mode. Using Eqs. (C1) and (C4) to (C7), the EKE and EPE can be expressed as:

$$K_e = \frac{1}{2}\rho_0 {u'_\theta}^2 = \frac{2\rho_0 g^2}{{f_0}^2} \cdot \frac{r^2}{R^4} H^2 {\eta'}^2, \tag{C8}$$

$$P_e = \frac{1}{2}\frac{g^2}{\rho_0 N^2}{\rho'}^2 = \frac{g^2}{2\rho_0 N^2} \cdot \alpha^2 {\eta'}^2. \tag{C9}$$

The volume-integral EKE and EPE are given by:

$$\begin{aligned} \mathcal{K} &= \frac{1}{2}\rho_0 \int_{z_{ref}}^{0} H^2(z)dz \int_0^{2\pi} d\theta \int_0^R {u'_\theta}^2 r dr \\ &= (1-3e^{-2}) \cdot \frac{\rho_0 g^2}{2{f_0}^2} \cdot \pi A^2 \int_{z_{ref}}^{0} H^2(z)dz \end{aligned} \tag{C10}$$

$$\mathcal{P} = \frac{g^2}{2\rho_0}\int_{z_{ref}}^{0}\frac{\alpha^2}{N^2}dz \iint_0^R {\eta'}^2 r dr = (1-e^{-2}) \cdot \frac{g^2}{4\rho_0} \cdot \pi R^2 A^2 \int_{z_{ref}}^{0}\frac{\alpha^2}{N^2}dz. \tag{C11}$$

Acknowledgments

This work was jointly supported by the Strategic Priority Research Program of the Chinese Academy of Sciences (XDA0370101), the National Natural Science Foundation of China (42276015, 42227901, 42106008, 42376019 and 42276022), Youth Innovation Promotion Association CAS (2019336), the National Key R&D Program of China (2023YFF0805300), the Natural Science Foundation of Guangdong Province (2021A1515012538, 2021A1515011613, 2023A1515011023 and 2024A1515012549), the Guangzhou Science and Technology Program 2024A04J9022, the Zhejiang Provincial Natural Science Foundation of China (LY24D060003), the Key R&D Program of Zhejiang Province (2024C03257), LASG Open Research Program (20220085) and the Open Project Program of State Key Laboratory of Tropical Oceanography (LTOZZ2002), the Basic Frontiers and Innovative Development 2023 "Integration" Project of South China Sea Institute of Oceanology (SCSIO2023QY02). Y. H. was supported by the State Key Laboratory of Satellite Ocean Environment Dynamics, SIO, MNR (QNHX2314), and acknowledges support from the CAS for a visiting scholarship at the University of East Anglia. The data processing is supported by the High-Performance Computing Division in the South China Sea Institute of Oceanology.

Data Availability Statement

The Ssalto/Duacs altimeter products were produced and distributed by the Copernicus Marine and Environment Monitoring Service (CMEMS) (http://marine.copernicus.eu). The daily altimetric Mesoscale Eddy Trajectories Atlas product (META3.1exp DT allsat) are produced by SSALTO/DUACS and distributed by AVISO+ (https://www.aviso.altimetry.fr/) with support from CNES, in collaboration with IMEDEA. Argo data were collected and made freely available by the International Argo Program and the national programs that contribute to it. These data are download from the Coriolis Global Data Acquisition Center of France (ftp://ftp.ifremer.fr/ifremer/argo/geo/). The WOA 2018 data set can be found online (https://www.ncei.noaa.gov/data/oceans/woa/WOA18/DATA/).

References

Batteen, M. L., and C. L. Butler (1998), Modeling Studies of the Leeuwin Current off Western and Southern Australia, *J. Phys. Oceanogr.*, *28*(11), 2199-2221, doi:10.1175/1520-0485(1998)028<2199:MSOTLC>2.0.CO;2.

Boyer, Tim P.; Garcia, Hernan E.; Locarnini, Ricardo A.; Zweng, Melissa M.; Mishonov, Alexey V.; Reagan, James R.; Weathers, Katharine A.; Baranova, Olga K.; Seidov, Dan; Smolyar, Igor V. (2018). World Ocean Atlas 2018. Temperature and Salinity. NOAA National Centers for Environmental Information. Dataset. https://www.ncei.noaa.gov/archive/accession/NCEI-WOA18.

Chaigneau, A., M. Le Texier, G. Eldin, C. Grados, and O. Pizarro (2011), Vertical structure of mesoscale eddies in the eastern South Pacific Ocean: A composite analysis from altimetry and Argo profiling floats, *Journal of Geophysical Research: Oceans*, *116*(C11), C11025, doi:10.1029/2011jc007134.

Chelton, D. B., R. A. deSzoeke, M. G. Schlax, K. El Naggar, and N. Siwertz (1998), Geographical Variability of the First Baroclinic Rossby Radius of Deformation, *J. Phys. Oceanogr.*, *28*(3), 433-460, doi:10.1175/1520-0485(1998)028<0433:GVOTFB>2.0.CO;2.

Chen, G., Y. Hou, and X. Chu (2011), Mesoscale eddies in the South China Sea: Mean properties, spatiotemporal variability, and impact on thermohaline structure, *J. Geophys. Res.*, *116*(C6), C06018, doi:10.1029/2010jc006716.

Chen, G., and G. Han (2019), Contrasting Short-Lived With Long-Lived Mesoscale Eddies in the Global Ocean, *Journal of Geophysical Research: Oceans*, *124*(5), 3149-3167, doi:https://doi.org/10.1029/2019JC014983.

Chen, R., G. R. Flierl, and C. Wunsch (2014), A Description of Local and Nonlocal Eddy–Mean Flow Interaction in a Global Eddy-Permitting State Estimate, *J. Phys. Oceanogr.*, *44*(9), 2336-2352, doi:https://doi.org/10.1175/JPO-D-14-0009.1.

Cushman-Roisin, B., and J.-M. Beckers (2011), Chapter 16 - Quasi-Geostrophic Dynamics, in *International Geophysics*, edited by B. Cushman-Roisin and J.-M. Beckers, pp. 521-551, Academic Press, doi:https://doi.org/10.1016/B978-0-12-088759-0.00016-X.

Dilmahamod, A. F., B. Aguiar-González, P. Penven, C. J. C. Reason, W. P. M. De Ruijter, N. Malan, and J. C. Hermes (2018), SIDDIES Corridor: A Major East-West Pathway of Long-Lived Surface and Subsurface Eddies Crossing the Subtropical South Indian Ocean, *Journal of Geophysical Research: Oceans*, *123*(8), 5406-5425, doi:10.1029/2018JC013828.

Dong, C., J. C. McWilliams, Y. Liu, and D. Chen (2014), Global heat and salt transports by eddy movement, *Nat Commun*, *5*, doi:10.1038/ncomms4294.

Dufois, F., N. J. Hardman-Mountford, J. Greenwood, A. J. Richardson, M. Feng, S. Herbette, and R. Matear (2014), Impact of eddies on surface chlorophyll in the South Indian Ocean, *Journal of Geophysical Research: Oceans*, *119*(11), 8061-8077, doi:10.1002/2014JC010164.

Early, J. J., R. M. Samelson, and D. B. Chelton (2011), The Evolution and Propagation of Quasigeostrophic Ocean Eddies, *J. Phys. Oceanogr.*, *41*(8), 1535-1555, doi:doi:10.1175/2011JPO4601.1.

Feng, M., S. Wijffels, S. Godfrey, and G. Meyers (2005), Do Eddies Play a Role in the Momentum Balance of the Leeuwin Current?, *J. Phys. Oceanogr.*, *35*(6), 964-975, doi:10.1175/JPO2730.1.

Feng, M., L. J. Majewski, C. B. Fandry, and A. M. Waite (2007), Characteristics of two counter-rotating eddies in the Leeuwin Current system off the Western Australian coast, *Deep Sea Research Part II: Topical Studies in Oceanography*, *54*(8–10), 961-980, doi:http://dx.doi.org/10.1016/j.dsr2.2006.11.022.

Ferrari, R., and C. Wunsch (2009), Ocean Circulation Kinetic Energy: Reservoirs, Sources, and Sinks, *Annual Review of Fluid Mechanics*, *41*(1), 253-282, doi:10.1146/annurev.fluid.40.111406.102139.

Gaube, P., D. B. Chelton, R. M. Samelson, M. G. Schlax, and L. W. O'Neill (2015), Satellite Observations of Mesoscale Eddy-Induced Ekman Pumping, *J. Phys. Oceanogr.*, *45*(1), 104-132, doi:10.1175/jpo-d-14-0032.1.

Gula, J., M. J. Molemaker, and J. C. McWilliams (2016), Topographic generation of submesoscale centrifugal instability and energy dissipation, *Nature Communications*, *7*(1), 12811, doi:10.1038/ncomms12811.

Guo, Y., Y. Li, F. Wang, Y. Wei, and Q. Xia (2020), Importance of Resolving Mesoscale Eddies in the Model Simulation of Ningaloo Niño, *Geophysical Research Letters*, *47*(14), e2020GL087998, doi:https://doi.org/10.1029/2020GL087998.

Kang, D., and E. N. Curchitser (2015), Energetics of Eddy–Mean Flow Interactions in the Gulf Stream Region, *J. Phys. Oceanogr.*, *45*(4), 1103-1120, doi:https://doi.org/10.1175/JPO-D-14-0200.1.

Kurian, J., F. Colas, X. Capet, J. C. McWilliams, and D. B. Chelton (2011), Eddy properties in the California Current System, *J. Geophys. Res.*, *116*(C8), C08027, doi:10.1029/2010jc006895.

He, Y., M. Feng, J. Xie, Q. He, J. Liu, J. Xu, Z. Chen, Y. Zhang, and S. Cai (2021), Revisit the Vertical Structure of the Eddies and Eddy-Induced Transport in the Leeuwin Current System, *Journal of Geophysical Research: Oceans*, *126*(4), e2020JC016556, doi:https://doi.org/10.1029/2020JC016556.

Huang, R. X. (2014), Energetics of lateral eddy diffusion/advection: Part II. Numerical diffusion/diffusivity and gravitational potential energy change due to isopycnal diffusion, *Acta Oceanologica Sinica*, *33*(3), 19-39, doi:10.1007/s13131-014-0410-0.

Ledwell, J. R., A. J. Watson, and C. S. Law (1998), Mixing of a tracer in the pycnocline, *J. Geophys. Res.*, 103(C10), 21499–21529, doi:10.1029/98JC01738.

Liu, T., and R. Abernathey (2023), A global Lagrangian eddy dataset based on satellite altimetry, *Earth Syst. Sci. Data*, *15*(4), 1765-1778, doi:10.5194/essd-15-1765-2023.

Liu, T., Y.-K. Qian, X. Liu, S. Peng, and D. Chen (2024), Irreversible Mixing Induced by Geostrophic Turbulence over the Global Ocean, *J. Phys. Oceanogr.*, *54*(3), 911-928, doi:https://doi.org/10.1175/JPO-D-23-0071.1.

Liu, Z., G. Liao, X. Hu, and B. Zhou (2020), Aspect Ratio of Eddies Inferred From Argo Floats and Satellite Altimeter Data in the Ocean, *Journal of Geophysical Research: Oceans*, *125*(1), e2019JC015555, doi:https://doi.org/10.1029/2019JC015555.

Lumpkin, R., A.-M. Treguier, and K. Speer (2002), Lagrangian Eddy Scales in the Northern Atlantic Ocean, *J. Phys. Oceanogr.*, *32*(9), 2425-2440, doi:https://doi.org/10.1175/1520-0485(2002)032<2425:LESITN>2.0.CO;2.

Jia, F., L. Wu, and B. Qiu (2011), Seasonal Modulation of Eddy Kinetic Energy and Its Formation Mechanism in the Southeast Indian Ocean, *J. Phys. Oceanogr.*, *41*(4), 657-665, doi:10.1175/2010jpo4436.1.

Mao, H., M. Feng, H. E. Phillips, and S. Lian (2019), Mesoscale eddy characteristics in the interior subtropical southeast Indian Ocean, tracked from the Leeuwin Current system, *Deep Sea Research Part II: Topical Studies in Oceanography*, *161*, 52-62, doi:https://doi.org/10.1016/j.dsr2.2018.07.003.

Mason, E., A. Pascual, and J. C. McWilliams (2014), A New Sea Surface Height–Based Code for Oceanic Mesoscale Eddy Tracking, *Journal of Atmospheric and Oceanic Technology*, *31*(5), 1181-1188, doi:https://doi.org/10.1175/JTECH-D-14-00019.1.

Morrow, R., F. Fang, M. Fieux, and R. Molcard (2003), Anatomy of three warm-core Leeuwin Current eddies, *Deep Sea Research Part II: Topical Studies in Oceanography*, *50*(12–13), 2229-2243, doi:https://doi.org/10.1016/S0967-0645(03)00054-7.

Nikurashin, M., G. K. Vallis, and A. Adcroft (2012), Routes to energy dissipation for geostrophic flows in the Southern Ocean, *Nat. Geosci.*, *6*, 48, doi:10.1038/ngeo1657.

Okubo, A. (1971), Oceanic diffusion diagrams, *Deep Sea Research and Oceanographic Abstracts*, *18*(8), 789-802, doi:https://doi.org/10.1016/0011-7471(71)90046-5.

Palastanga, V., P. J. van Leeuwen, M. W. Schouten, and W. P. M. de Ruijter (2007), Flow structure and variability in the subtropical Indian Ocean: Instability of the South Indian Ocean Countercurrent, *Journal of Geophysical Research: Oceans*, *112*(C1), doi:https://doi.org/10.1029/2005JC003395.

Patel, R. S., J. Llort, P. G. Strutton, H. E. Phillips, S. Moreau, P. Conde Pardo, and A. Lenton (2020), The Biogeochemical Structure of Southern Ocean Mesoscale Eddies, *Journal of Geophysical Research: Oceans*, *125*(8), e2020JC016115, doi:https://doi.org/10.1029/2020JC016115.

Pegliasco, C., A. Chaigneau, and R. Morrow (2015), Main eddy vertical structures observed in the four major Eastern Boundary Upwelling Systems, *Journal of Geophysical Research: Oceans*, *120*(9), 6008-6033, doi:10.1002/2015JC010950.

Pegliasco, C., Delepoulle, A., Mason, E., Morrow, R., Faugère, Y., Dibarboure, G., 2022. META3.1exp: a new global mesoscale eddy trajectory atlas derived from altimetry. Earth Syst. Sci. Data 14, 1087–1107. https://doi.org/10.5194/essd-14-1087-2022

Phillips, H. E., Tandon, A., Furue, R., Hood, R., Ummenhofer, C. C., Benthuysen, J. A., et al. (2021). Progress in understanding of Indian Ocean circulation, variability, air–sea exchange, and impacts on biogeochemistry. *Ocean Sci., 17*(6), 1677-1751.

Qian, Y.-K., S. Peng, and Y. Li (2013), Eulerian and Lagrangian Statistics in the South China Sea as Deduced from Surface Drifters, *J. Phys. Oceanogr.*, *43*(4), 726-743, doi:https://doi.org/10.1175/JPO-D-12-0170.1.

Qu, T., Z. Lian, X. Nie, and Z. Wei (2019), Eddy-Induced Meridional Salt Flux and Its Impacts on the Sea Surface Salinity Maxima in the Southern Subtropical Oceans, *Geophysical Research Letters*, *46*(20), 11292-11300, doi:10.1029/2019gl084807.

Rennie, S. J., C. P. Pattiaratchi, and R. D. McCauley (2007), Eddy formation through the interaction between the Leeuwin Current, Leeuwin Undercurrent and topography, *Deep Sea Research Part II: Topical Studies in Oceanography*, *54*(8), 818-836, doi:https://doi.org/10.1016/j.dsr2.2007.02.005.

Talley, L. D., G. L. Pickard, W. J. Emery, and J. H. Swift (2011), *Descriptive Physical Oceanography: An Introduction*, 6th ed., Academic Press, Boston, Mass.

von Storch, J.-S., C. Eden, I. Fast, H. Haak, D. Hernández-Deckers, E. Maier-Reimer, J. Marotzke, and D. Stammer (2012), An Estimate of the Lorenz Energy Cycle for the World Ocean Based on the STORM/NCEP Simulation, *J. Phys. Oceanogr.*, *42*(12), 2185-2205, doi:10.1175/jpo-d-12-079.1.

Wang, Z., Q. Li, L. Sun, S. Li, Y. Yang, and S. Liu (2015), The most typical shape of oceanic mesoscale eddies from global satellite sea level observations, *Frontiers of Earth Science*, *9*(2), 202-208, doi:10.1007/s11707-014-0478-z.

Wunsch, C., and R. Ferrari (2004), VERTICAL MIXING, ENERGY, AND THE GENERAL CIRCULATION OF THE OCEANS, *Annual Review of Fluid Mechanics*, *36*(1), 281-314, doi: 10.1146/annurev.fluid.36.050802.122121.

Xu, C., X. Zhai, and X.-D. Shang (2016), Work done by atmospheric winds on mesoscale ocean eddies, *Geophysical Research Letters*, *43*(23), 2016GL071275, doi:10.1002/2016GL071275.

Yan, X., D. Kang, E. N. Curchitser, X. Liu, C. Pang, and L. Zhang (2023), Seasonal Variability of Eddy Kinetic Energy along the Kuroshio Current, *J. Phys. Oceanogr.*, *53*(7), 1731-1752, doi:https://doi.org/10.1175/JPO-D-22-0155.1.

Yang, G., F. Wang, Y. Li, and P. Lin (2013), Mesoscale eddies in the northwestern subtropical Pacific Ocean: Statistical characteristics and three-dimensional structures, *Journal of Geophysical Research: Oceans*, *118*(4), 1906-1925, doi:10.1002/jgrc.20164.

Zhang, N., G. Liu, Q. Liu, S. Zheng, and W. Perrie (2020), Spatiotemporal variations of mesoscale eddies in the southeast Indian Ocean, *Journal of Geophysical Research: Oceans*, *125*, e2019JC015712, doi:10.1029/2019JC015712.

Zhang, Z., Y. Zhang, W. Wang, and R. X. Huang (2013), Universal structure of mesoscale eddies in the ocean, *Geophysical Research Letters*, *40*(14), 3677-3681, doi:10.1002/grl.50736.

Zhang, Z., W. Wang, and B. Qiu (2014), Oceanic mass transport by mesoscale eddies, *Science*, *345*(6194), 322-324, doi:10.1126/science.1252418.